Ceramics International 50 (2024) 43683–43698

Contents lists available at ScienceDirect

Ceramics International

journal homepage: www.elsevier.com/locate/ceramint

Evaluating refractory material performance in pyrometallurgical recycling of lithium-ion batteries under a reducing atmosphere

Lukas Wiszniewski [a,*], Irmtraud Marschall [b], Thomas Hochsteiner [a], Thomas McFarlane Hoad [a], Klaus Doschek-Held [a], Harald Raupenstrauch [a]

[a] Montanuniversität Leoben, Chair of Thermal Processing Technology, Leoben, Austria
[b] K1-MET GmbH, in cooperation with Montanuniversität Leoben, Chair of Ceramics, Leoben, Austria

ARTICLE INFO

Handling Editor: Dr P. Vincenzini

Keywords:
Batteries
Refractories (E)
SiC (C)
Crucible test
Pyrometallurgical recycling
InduRed

ABSTRACT

Pyrometallurgical recycling of lithium-ion batteries (LIB) has emerged as the go-to approach in industrial recycling solutions, yet it encounters significant challenges, such as lithium (Li) slagging. This study explores a reactor for pyrometallurgical recycling, that offers the potential to overcome this bottleneck by simultaneously recovering lithium and phosphorous (P) via the gas stream, more noble elements including cobalt (Co), nickel (Ni) and copper (Cu) as an alloy and less noble elements like aluminum (Al), calcium (Ca) and silicium (Si) as a slag. However, to enhance the efficiency and performance of this reactor, a critical focus is placed on evaluating refractory materials with reduced corrosion and diffusion characteristics. Already explored refractory materials, including aluminum oxide (Al_2O_3) or magnesium oxide (MgO), have exhibited severe issues, such as accelerated corrosion and diffusion rates, leading to diminished performance and compromised efficiency. To evaluate a more suitable refractory material for pyrometallurgical recycling of LIB, tests using silicon carbide (SiC), chromium(III)-oxide (Cr_2O_3) and zirconium dioxide (ZrO_2) were performed up to 1600 °C. The test results indicate that the investigated refractory materials offer distinct advantages and disadvantages. While SiC shows minimal to no wear by corrosion, Cr_2O_3 exhibits higher resistance to Li diffusion. Contrary, ZrO_2 experienced severe corrosion and crack formation, showing unsuitability for LIB recycling. Based on these findings, a continuously operated reactor could use different refractory materials in specific zones. While the degasification zone could benefit from Cr_2O_3's minimal diffusion properties, areas with intense contact between the crucible and melt could utilize SiC's corrosion resistance. However, partial oxidation at the outer surface of the SiC crucible led to the formation of SiO_2, another critical point to consider for scale-up plans, as it might influence the mechanical integrity long-term.

1. Introduction

In pursuing sustainable energy solutions, recycling lithium-ion batteries (LIB) has emerged as a critical process, particularly within the pyrometallurgical sector [1]. This method, favored for its robustness against varying input streams, is integral to recovering valuable metals from spent LIBs [2,3]. Alternative recycling routes for LIBs, such as hydro- and bio-hydrometallurgy, are often highly susceptible to a varying input stream. Therefore, only some are used as stand-alone recycling routes within the industry [4]. While in pyrometallurgical routes, the main focus is put on Nickel (Ni) and Cobalt (Co), due to their prevailing economic relevance, Lithium (Li) is most often being slagged and therefore economically lost [5]. With Li designated as a critical raw material by the European Union and establishment of a mandatory recycling quota of 80 % by 2031, the appeal of recycling Li has been significantly amplified [6]. This circumstance is further underscored by Li's fluctuating price dynamics, highlighting the strategic importance of securing its supply through recycling initiatives [7].

To address this impending concern, a pyrometallurgical recycling approach is being developed by the Chair of Thermal Processing Technologies at Montanuniversität Leoben, being able to circumvent the limitations encountered by currently used industrial recycling methods. The proposed process route with the InduRed reactor as the core principle is capable of recovering Li and Phosphorous (P) via the gaseous phase while simultaneously producing an alloy containing elements such as Ni, Co, Manganese (Mn), and Iron (Fe). The principle is based on

* Corresponding author. Chair of Thermal Processing Technology, Montanuniversität Leoben, Franz Josef-Str. 18, Leoben, 8700, Austria.
E-mail address: lukas.wiszniewski@unileoben.ac.at (L. Wiszniewski).

https://doi.org/10.1016/j.ceramint.2024.08.220
Received 30 April 2024; Received in revised form 8 August 2024; Accepted 13 August 2024
Available online 14 August 2024

the carbothermic reduction of the input material via an inductively heated packed bed [8]. Although the slagging of lithium has verifiably been shown to be suppressed, a significant unresolved issue is finding refractory materials that are stable against the highly aggressive components of LIBs [9].

Previous use of refractories, particularly aluminum oxide (Al_2O_3) [5,10] and magnesium oxide (MgO) [11], has exposed challenges in terms of corrosion mainly due to the formation of cobalt aluminates ($CoAl_2O_4$) [12,13] using Al_2O_3 as refractory material and lithium diffusion within the crucible walls using MgO [14]. Corrosion, generally defined as the chemical attack on refractory material by a liquid phase such as slag, metal or alloy, occurs when the melt infiltrates the refractory matrix, creating capillaries that weaken the material's mechanical strength [15]. During this process, the fine grain of the refractory is washed out leaving the coarse grain exposed. This process occurs due to the chemical reaction between the liquid slag and solid refractory phases. It continues until the saturation point of the slag or the metal bath occurs through the refractory material [16]. Such issues can lead to contamination of the input material and significantly impact refractory stability and reusability. Furthermore, diffusion-related constraints can hinder lithium removal rates, thereby diminishing the overall process efficiency [17].

The challenge in pyrometallurgical recycling of LIBs lies in identifying refractory materials that withstand aggressive conditions at high temperatures and minimize the diffusion and corrosion caused by the complex mix of materials in spent batteries. This statement can be supported by findings from Qu et al. [18], where pyrometallurgical recycling of LIB with MgO and Al_2O_3 refractory materials showed severe dissolution effects of the crucible materials in the alloy, leading to increased dynamic viscosities and ultimately decreased metal recovery rates [18].

Per definition, refractories are non-metallic ceramic materials capable of withstanding temperatures higher than 1500 °C per DIN 51 060, where the refractoriness is defined by the pyrometric cone equivalent [19]. Most modern refractories are based on one or more non-metallic oxides, which can be divided into basic and non-basic refractories. All basic products are based on either calcium oxide (CaO) or MgO, whereas non-basic materials are based on Al_2O_3, silicon dioxide (SiO_2) or zirconium oxide (ZrO_2) [20]. This is a fundamental differentiation, as the correct refractory material is often based on the basicity of the medium in contact with the lining. In the case of the InduRed Reactor, this is mainly a molten phase consisting of elements such as Co, Ni and Fe and a gaseous phase containing Li, P and carbon monoxide (CO) [21]. Especially the highly reductive CO atmosphere present within the InduRed must be considered, as CO can react with FeO in the lining material. The reaction leads to carbon production, which sits within the refractory structure, leading to a loss in mechanical strength and increased cracking [22]. This reaction can occur at iron contents below 0,1 wt% metallic Fe [21].

Furthermore, refractories are differentiated into shaped and unshaped products. Shaped products are generally defined as all products delivered with a predefined geometry, where the most common forms are bricks [23]. Unshaped products, also known as monolithics, contain a wide range of products such as plastics, ramming mixes, mortars and castables, using either a chemical or hydraulic bond. The materials used in this paper are all hydraulic bonded castables with hydraulic bonds, which are then shaped using vibration [23] The hydraulic bond gives a mechanical strength up to temperatures of approximately 600 °C. After that, a ceramic bond is necessary, achieved by firing the mixes at temperatures between 1200 °C and 1500 °C. The achieved ceramic bond allows a temperature resistance of up to 1800 °C depending on the used raw material [21]. For the crucibles used within this paper, an additional thermal treatment was applied, to achive the above decribed mechanical properties and is described in the section materials and methods.

This research seeks to identify refractory materials that can enhance the durability and longevity of the reactor, thereby contributing to the overall effectiveness and sustainability of the recycling process. For this purpose, suitable refractory material for the application in the InduRed reactor, crucible tests using silicon carbide (SiC), chromium(III)-oxide (Cr_2O_3), and zirconium dioxide (ZrO_2) were performed based on the standard DIN CEN/TS 15418 [24]. These tests are designed to evaluate the corrosion resistance of high-temperature ceramics. While these tests show quick results with a straightforward experimental setup, they have the disadvantage of showing rapid saturation of the liquid phase and halting any reactions as the input material volume is low compared to the reactor material [15]. Therefore, after evaluating the most suitable candidates within these pre-tests, melting experiments were conducted within the InduMelt reactor, a batch version of the InduRed reactor, using higher amounts of input material with an increased exposure time for a maximum stress test.

2. Materials and methods

The approach and the applied methodology for the different sampling and high-temperature trials are given in this chapter, while Fig. 1 should provide an overview of these actions.

2.1. Refractory materials

All refractory samples tested in this paper are castables that make use of a hydraulic bond, meaning the mix has a cement content that reacts with water to create a solid product. The mix is processed with a specified water content and cast into a polylactic acid (PLA) mold to create the test samples. After the casting, they are air dried for 24 h, after which they are tempered at 290 °C, while the heat up is run at 50 °C•h^{-1}. Once the peak temperature is reached, a holding time of 10 h is used to guarantee that the water is removed from the test samples. The cool down after the tempering is not controlled.

The tempered samples are then put in an electric resistance furnace and heated to 1500 °C with a heating rate (HR) of 150 °C•h^{-1}. If the test samples are fired in an oxidizing atmosphere, the holding time is 4 h and the sample is placed in the furnace. To establish a reducing atmosphere, the samples are placed within corundum boxes, which are subsequently densely packed with coal grits. This method ensures that the samples are enveloped within a low-oxygen environment, which is essential for certain chemical reactions to occur. Due to the packing method, the holding time is extended to 5 h to guarantee the temperature reaches the center of the box. The firing process is a crucial point in the production of castables as this is the point where the refractory bond is built up, giving the samples their strength.

Within this research, the following three materials as shown in Table 1 were used for thermal treatments with two different LIB materials.

- Silicon carbide (CARSIT 86-3-DE): SIC is known for its excellent thermal conductivity, mechanical strength, and resistance to thermal shock, making it a suitable candidate for environments where rapid temperature changes occur. However, its performance can be compromised in oxidative atmospheres at high temperatures, leading to a reduction in lifespan [17].
- Chromium(III)-oxide (DIDURIT RK64-3-DE): Cr_2O_3 refractories are valued for their robustness in corrosive environments, attributed to the formation of a protective Cr_2O_3 layer. They are typically employed in operations that involve contact with basic slags. Nonetheless, using Cr_2O_3 has raised environmental and health concerns due to the potential formation of hazardous hexavalent chromium compounds at elevated temperatures [25].
- Zirconium dioxide: ZrO_2 exhibits high melting points and superior resistance to slag attack, which makes it an attractive option for demanding applications. Its stability at high temperatures and resistance to crack propagation are beneficial for prolonged service

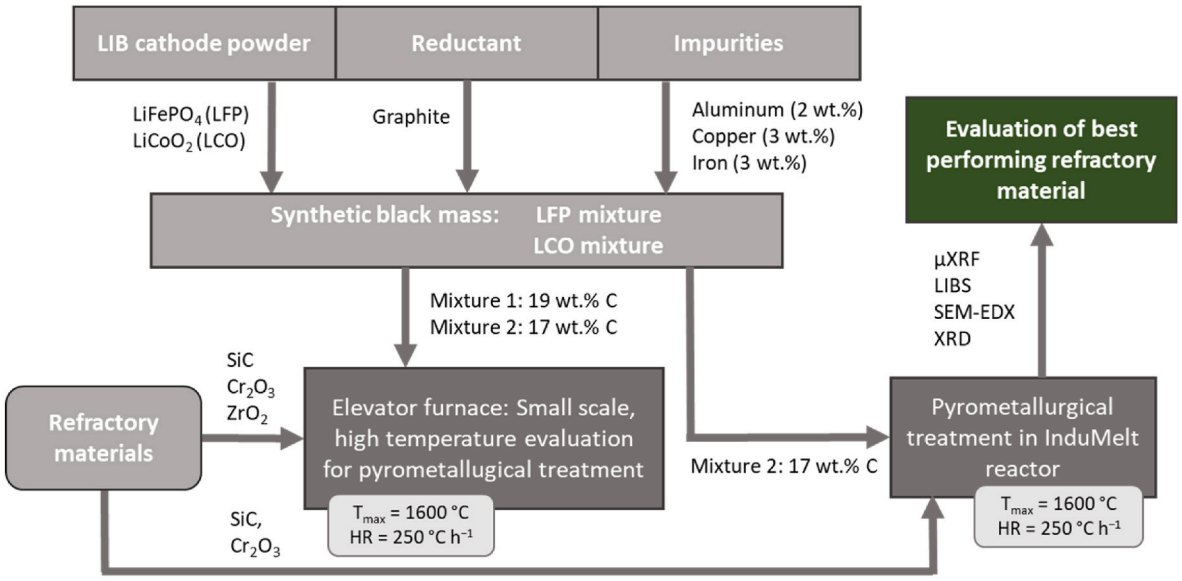

Fig. 1. Overview of the experimental procedure, including mixtures of the synthesized black mass, high-temperature reduction trials, and evaluation methods to find an optimum refractory material. [Silicon carbide (SiC), Chromium(III)-oxide (Cr_2O_3), Zirconium dioxide: ZrO_2, microscopic X-ray fluorescence analysis (µXRF), laser-induced breakdown spectroscopy (LIBS), scanning electron microscopy (SEM) and energy-dispersive X-ray spectroscopy (EDX), X-ray diffraction (XRD)]. (For interpretation of the references to color in this figure legend, the reader is referred to the Web version of this article.)

Table 1
Chemical composition of different refractory materials in wt.%.

Refractory material (wt.%)	Al_2O_3	SiO_2	Fe_2O_3	Cr_2O_3	SiC	TiO_2	FeO	CaO	K_2O	ZrO_2	MgO
Chrome corundum (Cr_2O_3)	25.0	4.8	0.5	64.0	–	1.7	0.9	1.5	–	–	–
Silicon carbide (SiC)	6.0	6.0	0.5	–	85.2	–	–	1.5	0.1	–	0.7
Zirconium oxide (ZrO_2)	6.0	6.0	0.5	–	–	–	–	1.5	0.1	86.0	–
Magnesium oxide (MgO)	0.1	0.5	–	–	–	–	–	1.1	–	–	97.5
Corundum (Al_2O_3)	99.7	<0.1	–	–	<0.1	–	–	–	–	–	–

life. However, zirconia can undergo phase transformations that may affect its thermal stability and mechanical integrity and must be considered when applying specific heating rates [26].

Further properties such as open porosity and bulk density are given in Table 2. These data are relevant for further discussion regarding possible diffusion and corrosion behavior of the different refractory materials.

2.2. Lithium-ion battery materials

Next to different refractory materials, two different LIB input materials were used to analyze the corrosion and diffusion behavior of different battery types. In order to simulate the black mass resulting from battery processing, pure cathode material from production (Gelon Energy Corp., Linyi, China) was mixed with several elements which can be found in the resulting black mass from battery processing. These additional elements typically result from mechanical pre-treatment steps such as crushing the batteries, which leaves residues of aluminum (Al) and copper (Cu) from the electrode conductor foils and Fe from the casing of the battery within the black mass. Additionally, carbon (C) was added to simulate the anode material, which typically consists of graphite [26,27]. To guarantee comparability between each test, the same concentrations of the above-mentioned elements were used. As reference material for black mass, pre-treated NCA-cells (Panasonic NCR 18650A— $LiNi_{0.8}Co_{0.15}Al_{0.05}O_2$) provided by Fraunhofer IWKS, Hanau, Germany, and several samples from spent LIBs analyzed via ICP-OES were used. The chemical composition and the concentrations of the before-mentioned elements of the Panasonic cells and the ICP-OES analysis of two of the other test cells are shown in Table 3.

The required quantity of graphite powder for a total reduction process was calculated based on the stoichiometry of the specific cathode material. Therefore, the mass of the cathode material was multiplied by the molar ratio of either $LiCoO_2$ or $LiFePO_4$. The number of moles of oxygen was then determined by multiplying the mass of oxygen by the atomic mass of oxygen. Following this, the necessary mass of carbon was calculated using the atomic mass of carbon and assuming that the carbon would be fully converted to carbon monoxide (CO) within the reactor. As the actual reaction products within the reactor will not only produce CO but also carbon dioxide (CO_2), the stoichiometrically needed amount

Table 2
Physical properties of the refratory materials after thermal treatment at 1500 °C.

	SiC	Cr_2O_3	ZrO_2
Bulk density/g*cm^{-3}	2.5	3.6	3.88
Open porosity/%	20.5	20.2	24
Cold bending strength/MPa	40	23	12
Cold pressure resistance/MPa	219	152	150

Table 3
Chemical composition of different black mass samples in wt.%.

Battery Type (wt.%)	Li	Co	Ni	Mn	Fe	P	C	Al	Cu
NCA[a]	3.4	5.0	31.0	–	2.7	–	34.6	2.4	3.6
NMC	2.8	14.5	5.9	4.2	0.6	0.6	31.2	5.3	3.5
LFP	2.5	0.1	0.4	0.1	17.7	10.2	29.2	1.7	5.8

[a] Data taken from Holzer et al., 2022 [27].

of carbon is likely lower. After these calculations, 20 wt% of C for the total reduction of $LiCoO_2$ and about 24 wt% of C for the reduction of $LiFePO_4$ would be needed, also previously calculated by Holzer et al. [11]. However, as also 2 wt% of Al and 3 wt% of Cu were added to the mixture to simulate an actual black mass, the higher reduction potential of Al compared to C would likely decrease the necessary amount of carbon. Therefore, 19 wt% and 17 wt% of carbon was used for the melting trials (Table 4).

The proportion of oxygen (O), elements with a lower concentration, particulary sulfur (S) as an impurity within the LFP cathode material and the carbon powder, or measurement uncertainties can explain deviations from the 100 % detection rate within Tables 3 and 4.

2.3. High temperature treatment – elevator furnace

In preliminary tests, standardized crucible tests were carried out to investigate the basic suitability of the crucible materials used and the influence of different cathode materials on corrosion and diffusion behavior. For this purpose, an electrically heated bottom-loading resistance furnace ("Thermconcept ELHT elevator furnace ELHT 16/18″) from Thermconcept, with a maximum heating rate of 600 °C•h^{-1} and a maximum temperature of 1800 °C, was used. The heating of the oven chamber is achieved through the utilization of ten heating elements composed of molybdenum disilicide. Furthermore, four inlets positioned within the electro-mechanically elevating bottom platform purge the oven chamber with 4 L per minute argon (Ar). For safety reasons, all samples were placed into a cylindrical graphite crucible with a graphite lid, with an inner diameter of 15 cm, an inner height of 12 cm, and a wall thickness of around 1.5 cm. This was done to avoid false air oxidation and to simulate a reducing atmosphere within the InduMelt reactor. In Fig. 2a and b, the furnace and the temperature profile of the oven applied for the test series are given [28].

The heating rate for the furnace was defined at 250 °C h^{-1} for SiC and Cr_2O_3 to simulate the current heating rate in the InduMelt reactor. Only the crucibles made of ZrO_2 were heated at 50 °C h^{-1} to avoid deformation by thermal hysteresis properties of the material [29]. After a holding time of 2 h, a cooling phase with 200 °C h^{-1} and 50 °C h^{-1} respectively was initiated until a temperature of 600 °C was reached. The Argon purging was turned off, and the furnace cooled down convectively until room temperature was reached. Afterward, the samples were removed from the furnace. In Fig. 2b, the cooling curve for ZrO_2 is not entirely depicted in order to avoid excessive distortion of the relationship with the cooling curve of SiC and Cr_2O_3. However, 50 °C h^{-1} was also applied until 600 °C was reached.

2.4. Pyrometallurgical treatment - InduMelt reactor

The core element of the recycling procedure for which the test series was conducted within this paper is the so-called InduMelt reactor. As described by Holzer et al. [11], the InduMelt reactor represents a batch version of the continuously operated InduRed reactor (Raupenstrauch et al.) [8]. The reactor, developed initially to recycle P from sewage sludge ashes (SSA), is an inductively heated carbon bed reactor with graphite cubes as susceptor material. Compared to conventional smelting facilities, the graphite cubes offer an enlarged surface area, resulting in short diffusion paths and times, simplifying the gasification of volatile elements such as Li and P. These short contact times are crucial to

Table 4
Chemical composition of battery materials used for high temperature treatment in wt.%.

Cathode Material (wt. %)	Li	Co	Fe	P	C	Al	Cu
LCO	5.3	43.9	3.0	–	17.0–19.0	2.0	3.0
LFP	3.2	–	27.7	13.1	17.0–19.0	2.0	3.0

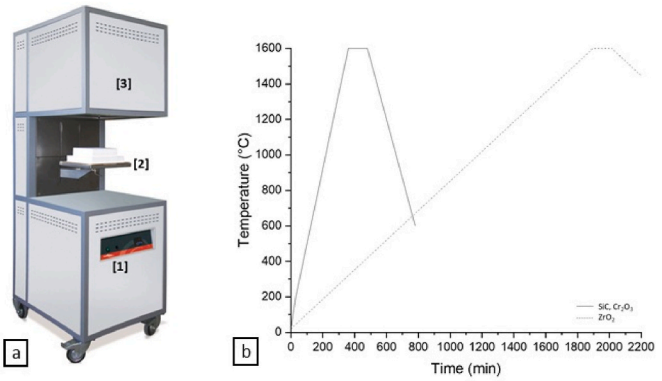

Fig. 2. a: Elevator furnace with [1] oven system temperature control (Eurotherm 3508) [2], elevating bottom platform with gas inlets [3], oven chamber; b: standardized temperature profiles for the crucible tests [28].

circumvent the slagging of Li or the formation of metal phosphides. Additional carbon is added to the input material for metal reduction and to avoid the wear of the graphite cubes. In the context of carbon oxidation, the equilibrium dynamics of the Boudouard reaction [30], accompanied by an excess reductant supply, lead to a reduction in the partial pressure of CO_2 above 700 °C within the reactor interior.

Consequently, a high CO/CO_2 ratio and a low partial pressure of O_2 can be assured, ensuring optimal conditions for reduction. The necessary heat to achieve the reaction temperature is generated by a copper induction coil placed around the crucible, with a maximum of 7.5 kW, inducing an eddy current in the graphite cubes, which leads to their heating via their ohmic resistance. The graphite cubes themselves have an electrical resistance of approximately 4–8 μΩ m with a side length of around 24.5 mm ± 1.5 mm and density ranging between 1.55 and 1.75 g cm^{-1}, exposed to a frequency of about 50 kHz. In Fig. 3a and b, technical drawings of the crucible of the InduMelt are given. The design for the Al_2O_3 crucible differs from that shown in Fig. 3, and can be seen in Holzer et al. [9].

To compare to previous trials conducted by Holzer et al. [9], the crucible is filled with four layers of 10–15 graphite cubes, with a third of the input material between each layer. Since all used refractory materials are at risk of thermal shock phenomena, the heating rate was limited to a maximum of 250 °C•h^{-1}. Monitored by three type K thermocouples located inside the reactor at the bottom, middle and top, and two type S thermocouples outside at the crucible surface, a maximum temperature of 1550 °C was reached after 8 h of heating. This heating period was then followed by a holding time of about 1 h to guarantee enough time for the complete reduction of the metal oxides and lithium evaporation. The crucible was insulated with two layers of refractory mats with a density of 128 kg m^{-3} and a thermal conductivity of 0.26 W mK^{-1} at 1000 °C to avoid heat losses. A new design for the gas vent was applied compared to the previous test series, in which an Al_2O_3 pipe was vertically uptight in the middle of the reactor between three layers of refractory mats. As seen in Fig. 4, a cylindrical lid made out of refractory concrete with concave curvature on the inside was put on top of the crucible to improve the extraction of gaseous components.

A gas wash bottle filled with distilled water removed lithium or other volatile elements from the gas stream. A water jet pump provided the necessary underpressure for the gas deduction.

Furthermore, the standardized sampling method described in Holzer et al. [9] was also slightly changed to better separate each fraction from another and achieve a more standardized procedure. Approximately 24 h after the end of the heating phase, once the crucible and interior were cooled down to room temperature, the graphite cubes and the solid fractions consisting of a metal alloy, a magnetic powder and a non-magnetic powder (slag), were removed and separated from each other via sieving up to a grain size of 0.5 mm and magnetic separation

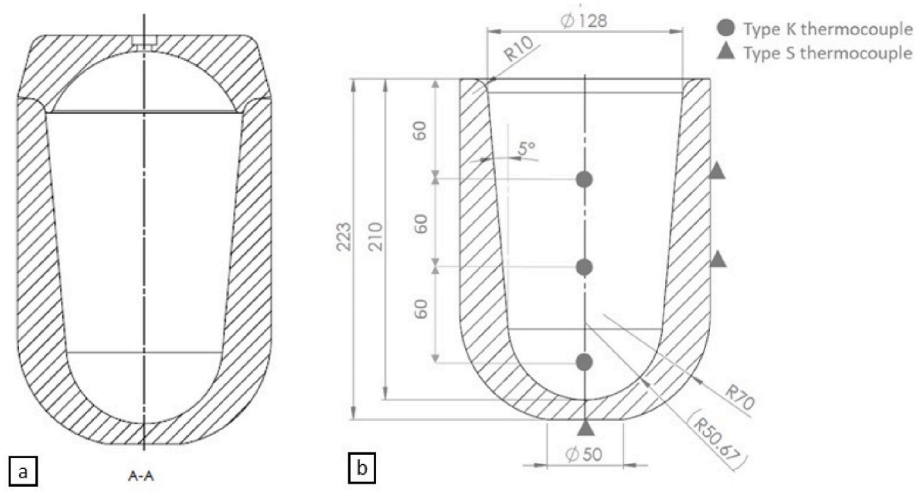

Fig. 3. Crucible design of the InduMelt reactor; a: crucible plus lid; b: crucible geometry with position of thermocouples.

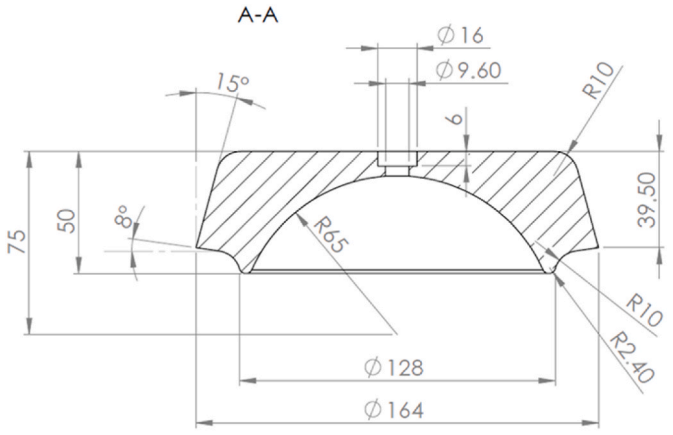

Fig. 4. Technical drawing of the lid used for the new design of InduMelt trials with improved gas extraction.

via a neodymium bar magnet. The metal fraction was then crushed with a jaw crusher with titanium jaws (Retsch BB 200 WC) to remove adherent sintered products from the metal surface. The resulting phases were again sieved and separated via a magnet and further analyzed with the methods described in the following chapter.

2.5. Analytical methods

Several characterization methods were applied to analyze the different solid fractions, from crucible materials and the metallic phases from the LIB mixtures. The crucibles from the standardized tests in the elevator furnace according to standard DIN CEN/TS 15418 and the crucible from the InduMelt trials were analyzed with microscopic X-ray fluorescence analysis (μXRF) with a Bruker M4 Tornado [31].

As μXRF analyses can only detect elements up to a periodic number of 11 (sodium), selected crucibles and metal phases were additionally analyzed regarding Li via laser-induced breakdown spectroscopy (LIBS; model EA-300, Keyence [optics 300x, laser–Nd: YAG 355 nm]) [32]. This was also done to provide a qualitative assumption of the depth of Li diffusion.

To examine features such as fractures within the surfaces or elemental compositions at the micrometer scale, scanning electron microscopy (SEM) and energy-dispersive X-ray spectroscopy (EDX) were used. In particular, a ZEISS EVO MA 15 with attached EDX from Oxford instruments (Ultimax 65) was used. With these tests several spectra were detected that could only be assigned to known phases with the addition of Li. To validate this assumption of phases, X-ray diffraction (XRD) measurements were done using a Bruker D8 advance in Bragg-Brentano geometry with Cu Kα radiation ($\lambda = 0.15418$ nm) at 25 mA and 40 kV. Diffraction patterns were collected in the 2θ range from 10° to 70° with a step size of 0.01° and 1 s acquisition time per step. XRD patterns were analyzed using the SIeve + software with PDF-4^{+} 2022 database (ICDD, USA).

Moreover, samples of the metallic and non-metallic fractions from the LIB input materials were investigated regarding their chemical composition via ICP-OES according to ÖNORM EN ISO 11885:200911 and X-ray fluorescence spectroscopy (XRF) [33]. This was done to compare the two analyzing methods and provide a database for future samples.

3. Results and discussion

Evaluating optimal refractory materials for pyrometallurgical recycling of LIBs has been critical in developing and continuously optimizing the InduMelt reactor. Preliminary tests were already conducted with aluminum oxide (Al_2O_3) and magnesium oxide (MgO) to assess their performance under reducing atmospheres, particularly in the presence of LIB materials, to identify a suitable candidate. The trials involving aluminum oxide unveiled a concerning outcome: the material exhibited a heightened susceptibility to severe corrosion under the reducing atmosphere of carbon monoxide (CO) and cobalt aluminate ($CoAl_2O_4$) formation. This corrosive attack led to the gradual degradation of the crucible, ultimately leading to destruction over time (https://www.mdpi.com/2227-9717/9/1/84). The pronounced reactivity of aluminum oxide under such conditions raises serious concerns regarding its feasibility as a refractory material for LIB pyrometallurgical recycling processes. The vulnerability to CO-induced corrosion and the formation of $CoAl_2O_4$ warrants careful consideration in selecting alternative materials to avoid compromising the integrity and longevity of the recycling setup, especially in a continuous process. In Fig. 5a and b, the deformation and corrosion behavior are illustrated.

Similarly, investigations involving MgO as a refractory material revealed significant diffusion issues when exposed to the reducing atmosphere and LIB cathode materials. Although almost no corrosion induced by cobalt or other elements nor by the reducing atmosphere was detected, over time, the crucible exhibited signs of dissolution after remaining at atmospheric conditions for several weeks, indicative of the detrimental effects of lithium-ion interactions on the material's stability. The diffusion problems encountered during these trials highlight potential challenges in maintaining magnesium oxide's structural integrity

Fig. 5. Crucibles before (a,c) and after (b, d) InduMelt trials; b): Al_2O_3 crucible with heavy corrosion signs (https://www.mdpi.com/2227-9717/9/1/84); d: MgO crucible with diffusion signs and cracks at the bottom (dimensions as seen within Fig. 3).

and durability in practical pyrometallurgical applications with LIB active material as input, asshown in Fig. 5c and d.

Additionally, as seen in Fig. 6, MgO suffered not only from severe Li diffusion which was confirmed by Holzer et al. [9], using the ICP-OES method, but also from P and Manganese (Mn) diffusion.

Given the critical role of refractory materials in preserving the integrity of the pyrometallurgical process, these observations underscore the necessity for an in-depth exploration of alternative candidates that can withstand the rigorous conditions inherent to LIB recycling. Materials capable of resisting CO-induced corrosion and LIB cathode material interactions are paramount to ensuring sustained efficiency and longevity in recycling operations, especially within further scale-up steps and continuous reactor operation.

3.1. Pre-tests according to DIN CEN/TS 15418

Standardized pre-tests according to the Norm DIN CEN/TS 15418 were carried out to investigate alternative refractory materials in an elevator furnace. The crucibles were placed in a surrounding crucible consisting of pure carbon to avoid damage to the furnace itself and possible oxidation reactions due to false air. Additionally, this carbon crucible should provide a reducing atmosphere by partial oxidation, as is present within the InduMelt reactor. Each crucible material was employed for separate loading with these input materials to analyze the different battery materials' potential corrosive behavior and diffusion mechanism). Initially, 50 g of the LCO mixture was introduced into one set of three different crucible materials.Subsequently, a different set of crucibles was filled with 25 g of the LFP mixture for melting experiments. Notably, each crucible material was used only once throughout the experimental procedure. As a result of the lower bulk density, only 25 g of LFP was needed to reach the same level as LCO within the crucibles. Fig. 7shows the different crucible materials before and after the melting trials with LFP.

First trials using 19 wt% of C, led to incomplete melting of the material and, therefore, less contact between the melt and refractory material. However, using 19 wt% of C in the presence of 2 wt% of Al, representing an even more potent reducing agent as C, a potentially excessive carbon content leads to an incomplete fusion of the metals, yielding a predominantly sintered structure rather than a fully melted state. This observation highlights several interpretations and inferences regarding the role of carbon content and its intricate influence on the thermochemical equilibrium of the system, which has to be answered in future research activities. The evolution of gas-phase species in conjunction with the catalytic and reducing effect of carbon and other elements such as aluminum could lead to a dynamic equilibrium state, wherein the influence of sintering phenomena counterbalances the propensity for metal fusion. Moreover, it is noteworthy that the absence of pronounced corrosion and diffusion effects for most of the investigated materials could result from the lack of a fully molten state of the input material. Only within ZrO_2 did deformation occur, which results more likely from the reversible volume expansion phenomena caused by the tetragonal (<1170 °C) to monoclinic (1170 °C–2370 °C) transformation when being cooled down, rather than corrosive effects from the LIB active material. Although doping with certain oxides such as CaO leads to better form stability, the necessary cubic structure, which stays metastable during cooling phases, only appears at temperatures above 2370 °C (hysteresis curve). However, as the maximum temperature was only about 1600 °C within these test series, the occurring phase changes with volume expansions of about 8 %, inducing significant stresses and leading to crack formation [34]. Ultimately, the C content was reduced to 17 wt% as this mixture has provided a fully molten state within heating microscope trials conducted in previous work [35].

The results of the μXRF analyses, illustrated in Fig. 8, demonstrate a pronounced capacity of the distinct crucible materials to impede diffusion. Remarkably, the minimal incursion of iron and copper from the LIB input material was visible within the crucible matrix of SiC and ZrO_2. Only Cr_2O_3 showed severe peeling phenomena at the corner where the contact between iron and the refractory material was increased, indicating a rather unsuitable combination between LFP and Cr_2O_3. Regarding the observed half-spherical shapes of CaO and SiO_2 at the bottom of the ZrO_2 crucible, the phenomenon may arise from a combination of factors. The original composition of ZrO_2 crucibles encompassing SiO_2 and CaO could lead to localized reactions with the materials processed within the crucible at high temperatures. Thermodynamic considerations, the interplay of material interfaces, and heat transfer dynamics within the crucible environment might influence the distinct morphology of these compounds.

As previous tests with Al_2O_3 and MgO crucibles have shown, LCO was the most aggressive material, probably due to its high cobalt content. Therefore, the same crucibles test as the LFP mixtures as input material have been conducted with the LCO mixture. The only difference between the two test series was the different amount of input material, as the LCO material got almost double the density as LFP and therefore needed 50 g instead of 25 g to reach the same level as LFP. Additionally, 50 g of the LFP mixture would have caused the crucible to

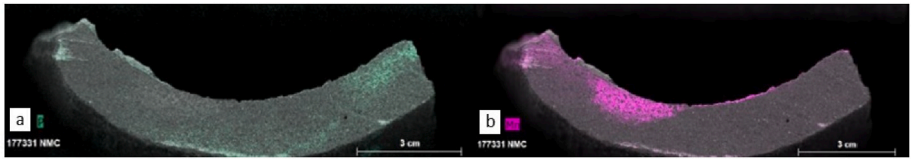

Fig. 6. Fragment of a MgO crucible after carbothermal reduction of $LiNi_{0.8}Mn_{0.1}Co_{0.1}O_2$ (NMC811) within the InduMelt reactor: a.) diffusion patterns of P; b.) diffusion patterns of Mn.

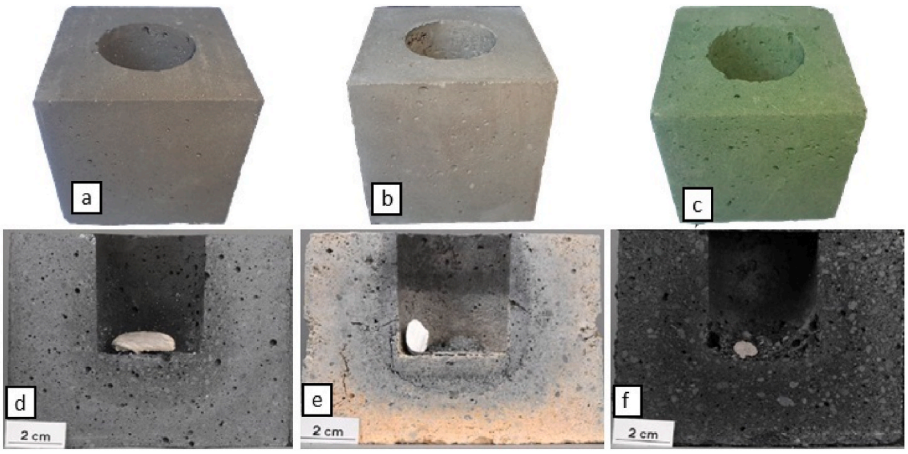

Fig. 7. Crucible materials before (a–c) and after (d–f) melting trials with LFP mixture: (a&d): SiC burned in reducing atmosphere; (b&e): ZrO_2 burned in oxidizing atmosphere; (c&f): Cr_2O_3 burned in oxidizing atmosphere.

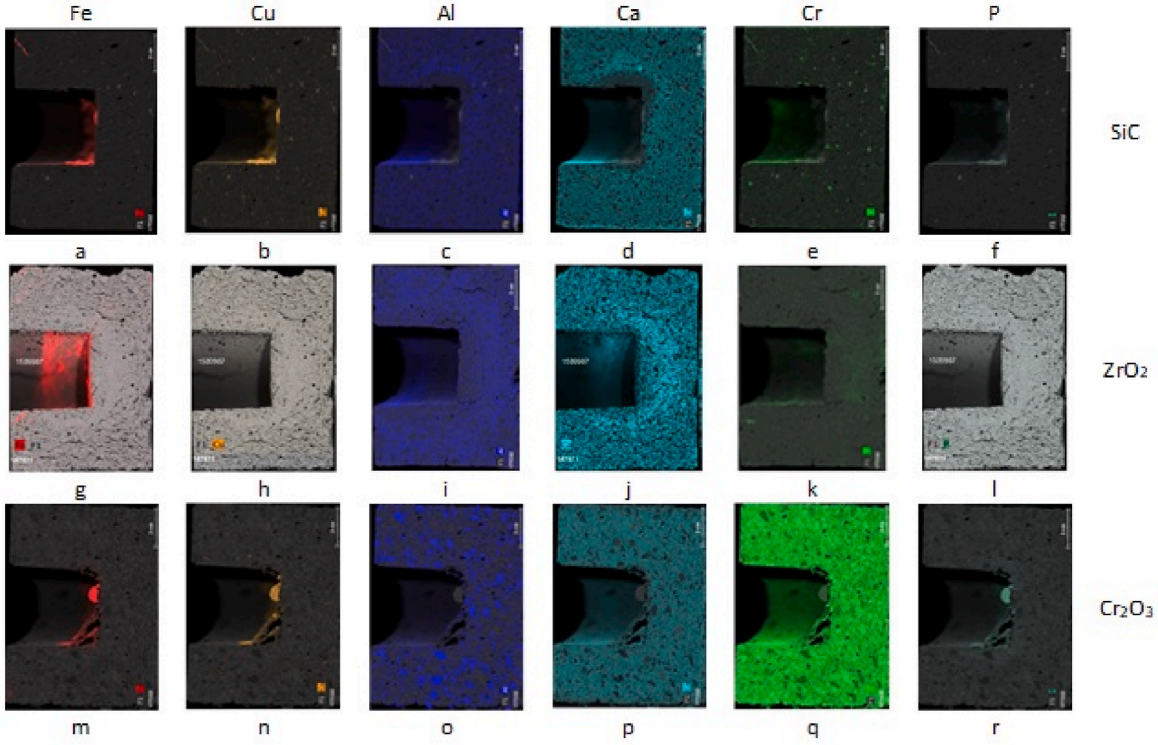

Fig. 8. µXRF analyses of different crucible materials regarding Fe, Cu, Al, Ca, Cr and P after treatment with LFP mixture: (a–f): elemental distribution within SiC; (g–l): elemental distribution within ZrO_2; (m–r) elemental distribution within Cr_2O_3.

overflow, so a defined volume as a reference was chosen rather than a mass. Fig. 9 shows an overview of the different crucibles before and after the high-temperature tests with the LCO mixture as input material, already showing a tendency towards SiC as the most prominent material regarding corrosion and temperature resistance.

Consistent with previous experimental observations utilizing the LFP mixture, the SiC crucible demonstrated enhanced resistance to corrosive degradation when exposed to the LCO mixture and exhibited stability under conditions of elevated thermal stress. There is also minimal evidence of diffusion on the sectioned interfaces of the crucibles, which is confirmed by the µXRF analyses shown in Fig. 10. Regarding SiC, however, sulfur penetration into the crucible materials could be attributed to the interactions between evaporated sulfur from impurities and other volatile elements such as Li. It might represent a potential risk to the stability of the crucible, especially within a continuous operation of an up-scaled version of the InduMelt. Given conditions such as high temperature and the reducing atmosphere dominated by CO, the formation of silicon sulfides is improbable due to the low partial pressure of sulfur, as only minor amounts of S were part of the input material. However, with a moderate partial pressure of Li, S may react with available Li to form lithium sulfide (Li2S) according to reaction 1, which is stable even at high temperatures [36].

$$2\,Li\,(g) + S\,(g) \rightarrow Li_2S\,(s) \qquad 1$$

The high temperature of 1600 °C can significantly increase the mobility of these molecules, even at low partial pressure. Additionally, defects in the SiC crystal structure, such as vacancies, dislocations, or grain boundaries, can provide pathways for sulfur diffusion. These

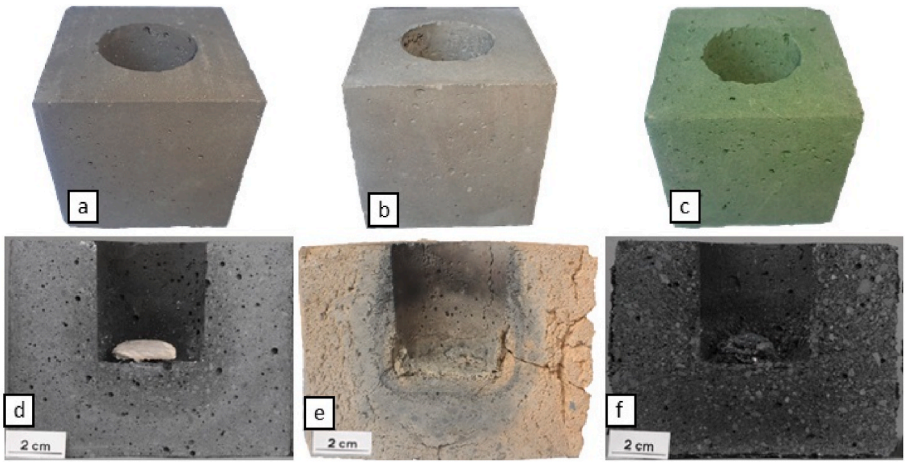

Fig. 9. Crucible materials before and after melting trials with LCO mixture: (a&c): SiC burned in reducing atmosphere; (b&e): ZrO_2 burned in oxidizing atmosphere; (c&f): Cr_2O_3 burned in oxidizing atmosphere.

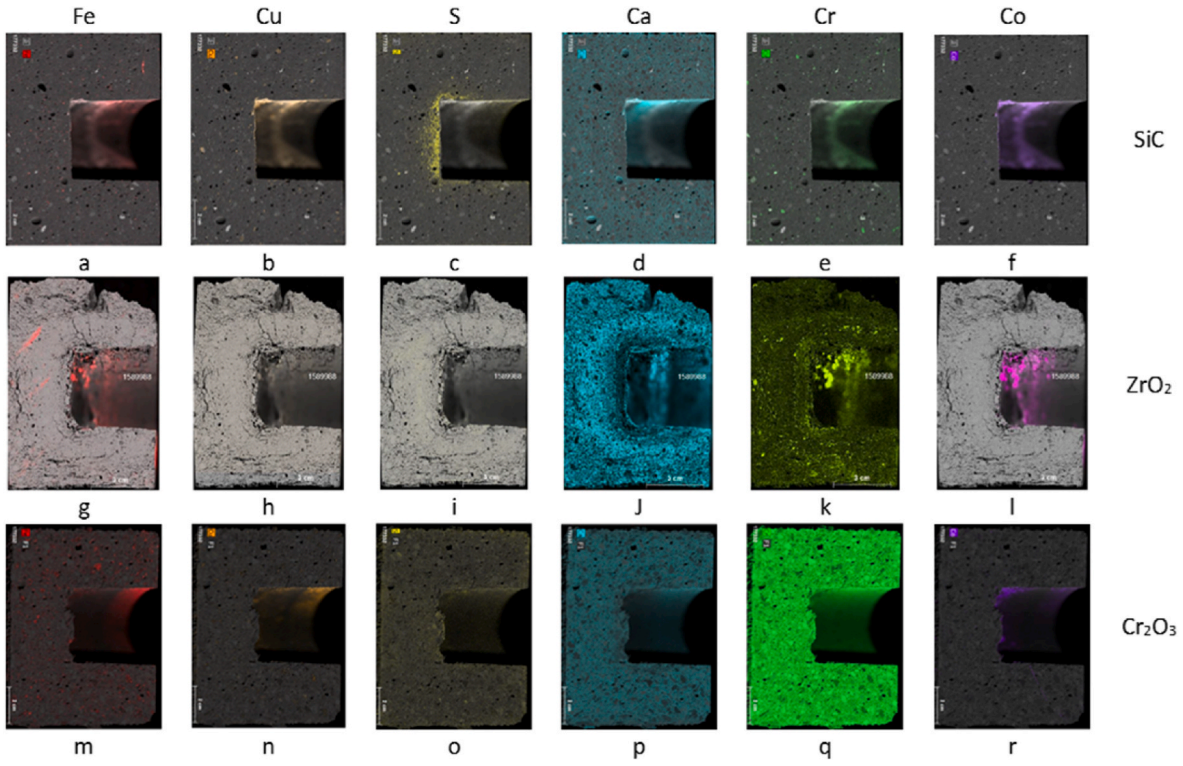

Fig. 10. μXRF analyses of different crucible materials regarding Fe, Cu, S, Ca, Cr and Co after contact with the LCO mixture: (a–f): elemental distribution within SiC; (g–l): elemental distribution within ZrO_2; (m–r) elemental distribution within Cr_2O_3.

defects can significantly enhance the diffusion rate compared to what would be expected in a perfect crystal lattice.

In contrast, the trials involving ZrO_2 crucibles exhibited pronounced crack development, which is likely attributable to the previously described hysteresis phenomena characterized by reversible volumetric expansion. Furthermore, the basal region of the reactor showed significant corrosive deterioration where the liquefied phase established direct contact with the crucible boundaries. This outcome again proved that ZrO_2 is not a suitable candidate as a refractory material for use in high temperatures under reducing atmospheres when in contact with LIB material.

Looking at the SiC crucibles' ability to avoid Li diffusion, Fig. 11 shows the LIBS analyses depending on the penetration depth horizontally and vertically. The point 0/0 in Fig. 11c represents the point marked by a yellow rectangle in Fig. 11b. From this point, every 3 mm in the horizontal and vertical direction, three measurements up to a depth of 9 mm have been taken (e.g.: 3/0 means 3 mm in the negative x-axis and 0 mm in the y-axis). As visualized in Fig. 11, Li was only found up to a depth of 3 mm, suggesting excellent diffusion barriers for Li in SiC.

The standardized tests yielded conclusive results, with SiC and Cr_2O_3 emerging as the superior materials due to their minimal corrosion and diffusion characteristics. Conversely, ZrO_2 consistently exhibited significant deformation and corrosion across all experiments. As previously described, phases changes in ZrO_2 could potentially lead to crack development during cooling. However, as XRD analyses (Fig. 12) of the new and used ZrO_2 crucibles show, both spectra reflects the XRD-pattern of the monoclinic Baddeleyte. Phase transition during heating and cooling is most likely. Further research, whether the volume changes or

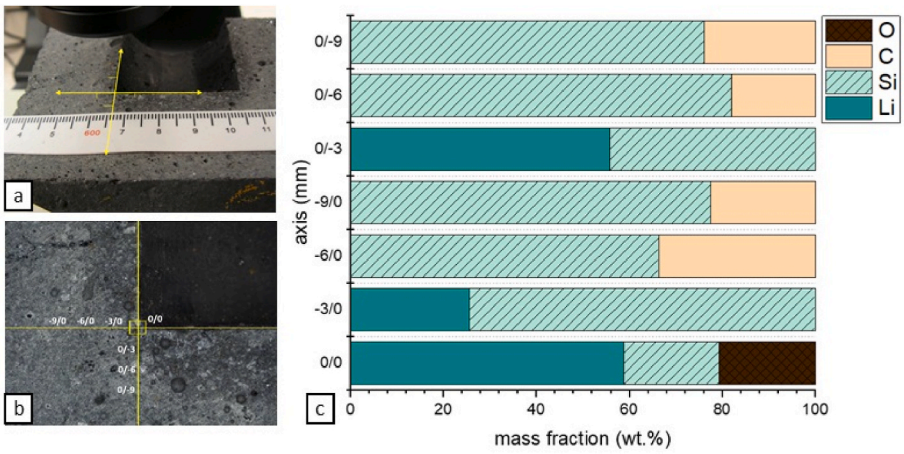

Fig. 11. Li diffusion behavior in SiC crucible with LCO mixture: a.) cross-section of the full crucible with coordinates; b.) illustrated point 0/0 with 300x magnification; c.) semi-quantitative mapping of horizontal and vertical points within the crucible.

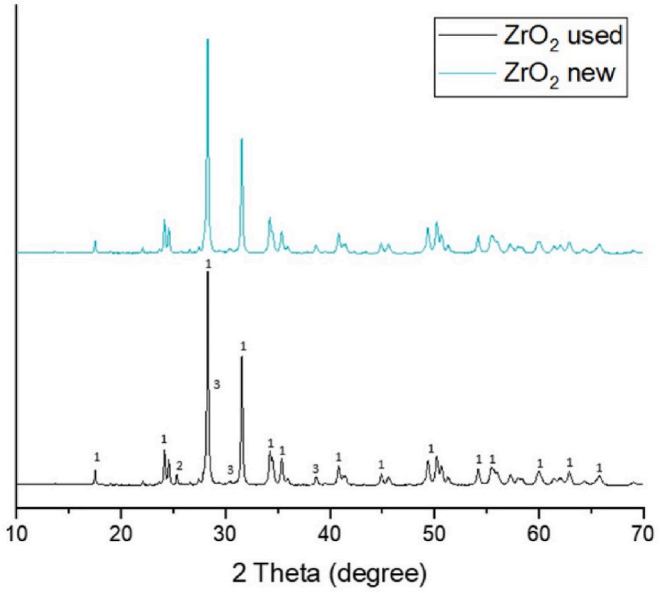

Fig. 12. XRD spectra of used and new ZrO_2 crucibles with 3 major phases: 1: ZrO_2 (Baddeleyte), 2: $LiAlSiO_4$, 3: $CaAl_2Si_2O_8$.

corrosive and infiltrative effects caused the cracking of the crucible have to be done. The only difference between used and new crucible is the formation of lithium aluminium silicates, which might lead to a weakening of the crucible. However, as first visual inspections provided enough data for proving unsuitability of ZrO_2 as refractory material for these tests, no further research regarding ZrO_2 is done within this paper.

To determine whether SiC and Cr_2O_3 can endure the more extreme conditions in the Indumelt reactor, crucibles composed of SiC and Cr_2O_3 were fabricated using a 3D-printed mold. Using these crucible molds, the specific geometries depicted in Figs. 3 and 4 are replicated. The outcomes of these subsequent trials, employing the same input material as utilized in the standardized tests, will be discussed in the following chapter, shedding light on their performance under the intensified operational conditions of the InduMelt reactor.

3.2. Carbothermal reduction test series within the InduMelt reactor

Building upon the insights gathered from the standardized tests based on norm DIN CEN/TS 15418, several insights could be derived. SiC and Cr_2O_3 outperformed ZrO_2 in terms of corrosion and diffusion resistance when exposed to different battery materials as input. ZrO_2 was prone to cracking and exhibited a marked susceptibility to corrosive attack with LCO as input material. It is essential to transition to the InduMelt trials, reflecting on these findings and considering their implications for the materials' behavior under the plant's more demanding operational conditions, such as local temperature hot-spots and higher CO partial pressure. Both SiC and Cr_2O_3 demonstrated excellent resistance to thermal stress, showing no significant thermal cracking or other degradation under the high-temperature cycles of the standardized tests. However, during the standardized tests, Cr_2O_3 allowed for a considerable phosphorous diffusion, while SiC exhibited sulfur diffusion. These diffusion phenomena are critical to understanding as they may influence the materials' integrity and performance in the long term.

Additionally, Cr_2O_3 showed slight peeling when interacting with LFP, resulting in iron and phosphorous infiltration, which could affect material selection depending on the input materials used in the InduMelt reactor. Generally, this performance suggests that both SiC and Cr_2O_3 are potentially well-suited to withstand the thermal stresses of the InduMelt reactor environment. Starting with SiC, Fig. 13 provides a visual representation of the crucible after carbothermal treatment of the LCO mixture.

Fig. 13 captures the complete crucible, including the lid, with remnants of ceramic fiber mat adhering to it. This is indicative of partial oxidation of the SiC surface outside the crucible. If this oxidation forms a protective layer, it could inhibit further oxidation and protect the material's core, a hypothesis that warrants further examination. The change in surface texture, from smooth to significantly rougher, is also evident and may affect the crucible's performance when the oxidation of the outer layer continues over time. The attack on the inner layer and the whole crucible is again mapped via μXRF analysis in Fig. 13.

As can be seen from Fig. 13, neither Co, Fe, or Cu infiltrated the SiC matrix, indicating extreme corrosion resistance against the LCO mixture, even under a highly reductive atmosphere with increased input material. Also, within the lid, no corrosion and diffusion effects were detected with μXRF analyses, so the figures are not shown in more details. Continuing with the performance of SiC, Fig. 14 shows the crucible after carbothermal treatment of the LFP mixture.

Similarly, in this experiment, the ceramic fiber mat adhered to the crucible's exterior surface after thermal treatment, supporting the hypothesis of partial oxidation occurring at the outer surface, where the O_2 partial pressure is high. LIBS analyses, revealed areas composed solely of silica and oxygen, further confirming the potential reaction between SiC and O_2 according to equation (2) [37].

$$SiC\ (s) + 2O_2\ (g) \rightarrow SiO_2\ (s) + CO_2\ (g)\ \Delta G_{1627\ ^\circ C} = -901.2\ kJ\ mol^{-1}\ 2$$

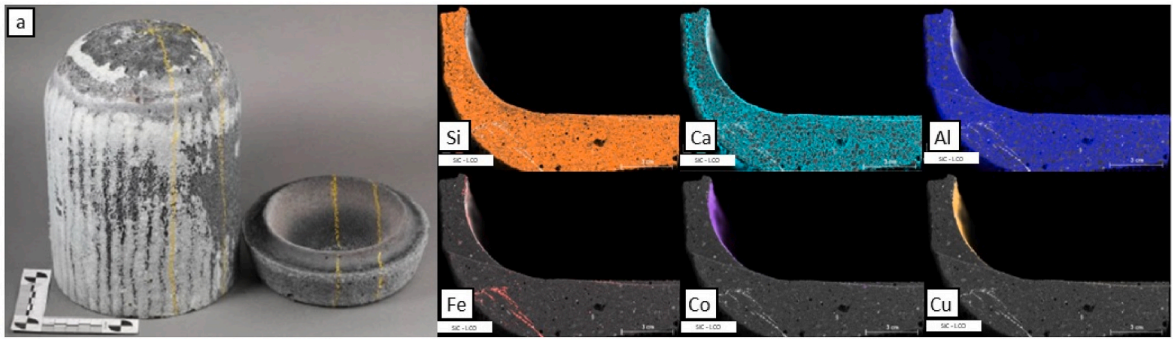

Fig. 13. SiC crucible and lid after carbothermal reduction of the LCO mixture: a.) crucible and lid with remnants of insulation wool; μXRF mapping of the elements Cr, Ca, Al, Fe, P and Cu of the bottom and the wall of the crucible.

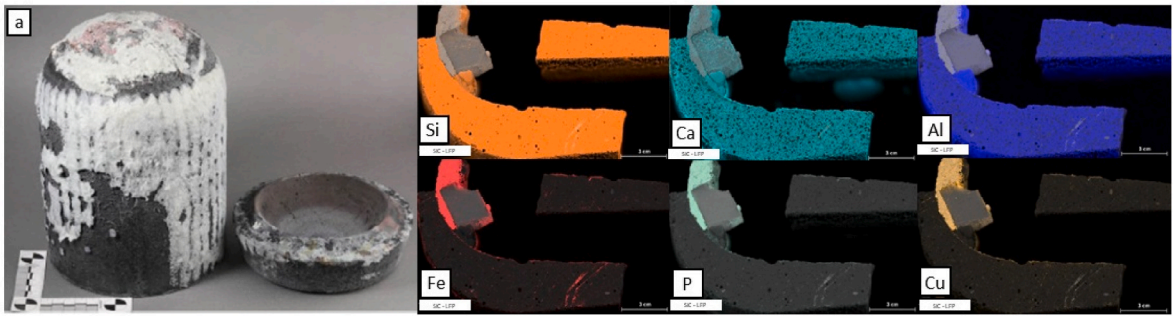

Fig. 14. SiC crucible and lid after carbothermal reduction of the LFP mixture: a.) crucible and lid with remnants of insulation wool; μXRF mapping of the elements Cr, Ca, Al, Fe, P and Cu of the bottom and the wall of the crucible.

This reaction is more likely to happen than the reaction stated in equation (3), as SiO_2 and CO_2 products are very stable compounds with strong Si–O and C–O bonds, which results in a significant release of energy.

$$SiC\ (s) + O_2\ (g) \rightarrow Si\ (s) + CO_2\ (g)\ \Delta G_{1627\ ^\circ C} = -361.9\ kJ\ mol^{-1} \quad 3$$

As the oxidation process of SiC has been subject to investigation for several decades, precise thermokinetic studies are available, which suggest a passive and active oxidation process of SiC [38]. Summarizing these studies, a passive oxidation is present, unless the partial pressure of oxygen is less than a critical value at a given temperature. Alternatively, a distinct transition temperature can be identified, were below passive oxidation predominates, accompanied by a mass increase [39]. The increase in mass after the trials, therefore most likely suggests a passive oxidation. This finding is crucial for long-term experiments as the mechanical strength of an already corroded material can change significantly compared to its original state. While active oxidation could lead to surface or subsurface defect density, decreasing the average flexural strength, passive oxidation could have a beneficial effect by healing surface cracks with layers of SiO_2 [38]. Furthermore, an essential factor for a continuous approach still to be investigated within the InduMelt and InduRed reactor are possible time-dependent effects such as creep and slow crack growth [40].

Initial visual examination revealed no thermal wear on the crucible, such as cracking or pronounced corrosion. Micro XRF analyses from Fig. 14 supported these initial findings, showing no evidence of corrosive interaction from either iron or copper or any phosphorus diffusion within the material.

Another important finding is the segregation between an obvious slag phase of Si, Ca and Al and the metal phase of Fe, Cu, and P where P is most likely present as Fe_2P or Fe_3P, according to Gibbs Energy. Regrding the Cr_2O_3 crucible, if metallic Cr forms, P has a higher affinity to Cr compared to Fe, most likely to form Cr_3P or CrP [41]. However, as the formation of Cr only happens at higher temperatures, where potential iron oxides have already been reduced, iron phosphides are more likely to be expected, mainly when most of the phosphorous at this temperature level should already have been extracted via the gas stream.

Compared to the trials with SiC as a refractory material, the trials with Cr_2O_3 had no visual signs of outer surface change as no ceramic fiber mat adhered to the crucible. However, after both trials with the LCO and LFP mixture, the Cr_2O_3 crucibles showed severe damage and crack formation. Fig. 15 shows the damage at the bottom of the reactor after the carbothermal reduction of the LCO mixture. Visual signs and μXRF analyses, shown in Fig. 15, revealed that minor corrosion effects occurred after the holding time of 4 h, leading to a pealing of the crucibles' inner wall. Additionally, 0.24 wt% of Cr was found in representative samples of the alloy, analyzed via XRF, which leads to the assumption of minor dissolution of the refractory material into the alloy.

However, after carbothermal reduction, tremendous corrosion, infiltration, and diffusion effects were observed between the LFP mixture and Cr_2O_3. As shown in Fig. 16, the outer visual appearance has changed in the bottom area, where a partial destruction of the crucible can be seen. Micro XRF analyses show deep infiltration of iron throughout the bottom of the crucible accompanied by P either as part of Fe_3P or via gaseous diffusion up to a depth of about 85 % of the width of the crucible.

After high-temperature treatment, XRF analysis showed 2.52 wt% of Cr in a representative sample of the alloy, indicating a stronger reaction between the crucible and input material than the LCO mixture with partial reduction of the Cr_2O_3. When looking at possible thermodynamic reactions occurring under elevated temperatures and a highly reducing atmosphere, carbothermic reduction of Cr_2O_3 at the inner layer of the crucible is to be expected. The carbothermic reduction of Cr_2O_3 has been extensively studied by different researchers, with some explicitly focusing on carbide formation summarized by Tomoyuki et al. (2007) [42] and Kryukov et al. (2019) [43]. The mechanism however, is complex due to the formation of three types of carbides and the evolving

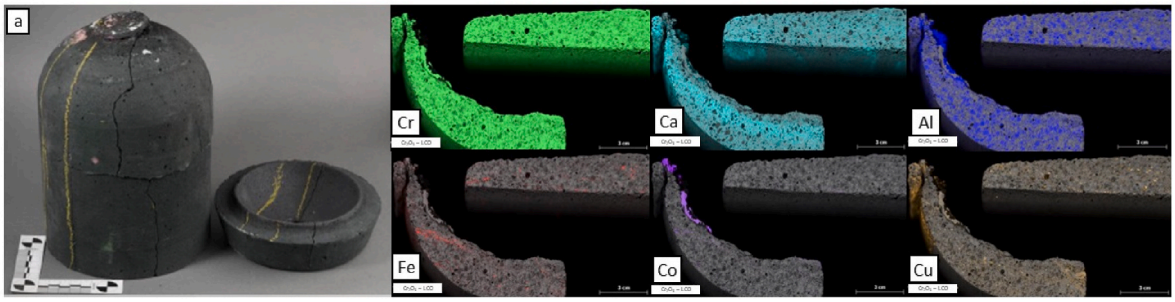

Fig. 15. Cr_2O_3 crucible and lid after carbothermal reduction of the LCO mixture: a.) crucible and lid with cracks; μXRF mapping of the elements Cr, Ca, Al, Fe, P and Cu of the bottom and the wall of the crucible.

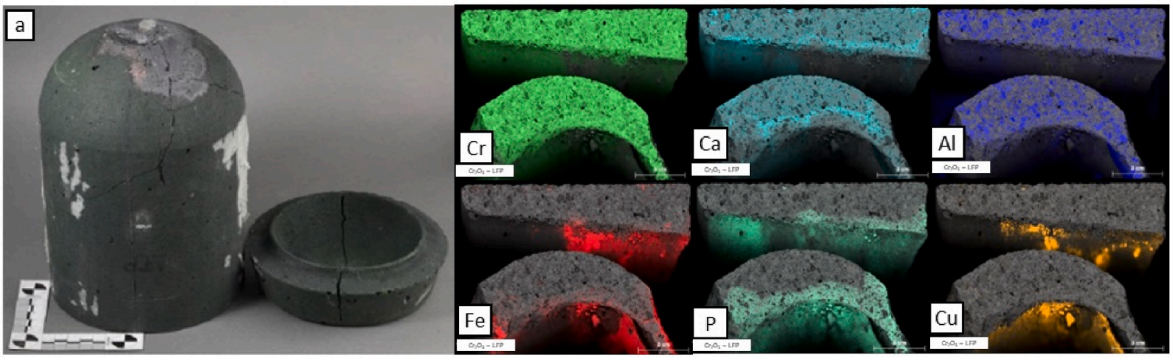

Fig. 16. Cr_2O_3 crucible and lid after carbothermal reduction of the LFP mixture: a.) crucible and lid with remnants of insulation wool; μXRF mapping of the elements Cr, Ca, Al, Fe, P and Cu of the bottom and the wall of the crucible.

nature of the reduction reaction as it progresses. Formula 4–6 describes the formation of the three carbides that exist in the Cr–C phase diagram with specific Gibbs energy except for the formation of Cr_3C_2, where no data was found.

$$3Cr_2O_3\ (s) + 13C\ (g) \rightarrow 2Cr_3C_2(s) + 9CO\ (g) \quad 4$$

$$7Cr_2O_3\ (s) + 27C\ (g) \rightarrow 2Cr_7C_3(s) + 21CO\ (g)\ \Delta G_{1227\ ^\circ C} = -25.6\ kJ\ mol^{-1};\ \Delta G_{1727\ ^\circ C} = -86.9\ kJ\ mol^{-1} \quad 5$$

$$23Cr_2O_3\ (s) + 81C\ (g) \rightarrow 2Cr_{23}C_6(s) + 69CO\ (g)\ \Delta G_{1227\ ^\circ C} = -21.5\ kJ\ mol^{-1};\ \Delta G_{1727\ ^\circ C} = -88.0\ kJ\ mol^{-1} \quad 6$$

Compared with other group IVb-VIb carbides, chromium carbides decompose ($Cr_{23}C_6$ at 1577 °C) or melt (Cr_7C_3 at 1768 °C) at relatively low temperatures. Once carbides form, they can further react with the chromium oxide, to form metallic chromium. The reduction degree, however, is particularly dependet on time and temperature, where metallic chromium only forms at temperatures higher than 1327 °C after about 1 h, according to Tomoyuki et al. (2007) [42]. While the temperature on the inside of the crucible was higher than this temperature, the outer surface of the crucible stayed below this temperature. This led to a partially reduction, only on the inside of the crucible, while the outer surface remained in its original oxidation state as can be seen in Figs. 15 and 16. Additionally indirect reduction via CO could potentially occure, however as Gibbs energy indicates, this behavior is rather unlikely, as stated in formula 7-9 and chances decrease with increasing temperature [43].

$$3Cr_2O_3\ (s) + 17CO\ (g) \rightarrow 2Cr_3C_2(s) + 13CO_2\ (g)\ \Delta G_{1227\ ^\circ C} = 50.5\ kJ\ mol^{-1};\ \Delta G_{1727\ ^\circ C} = 73.2\ kJ\ mol^{-1} \quad 7$$

$$7Cr_2O_3\ (s) + 33CO\ (g) \rightarrow 2Cr_7C_3(s) + 27CO_2\ (g)\ \Delta G_{1227\ ^\circ C} = 53.7\ kJ\ mol^{-1};\ \Delta G_{1727\ ^\circ C} = 72.7\ kJ\ mol^{-1} \quad 8$$

$$23Cr_2O_3\ (s) + 93CO\ (g) \rightarrow 2Cr_{23}C_6(s) + 81CO_2\ (g)\ \Delta G_{1227\ ^\circ C} = 60.7\ kJ\ mol^{-1};\ \Delta G_{1727\ ^\circ C} = 76.4\ kJ\ mol^{-1} \quad 9$$

Looking at possible reactions between S and SiC after carbothermal reduction of the LCO mixture, the findings of the pre-tests could be repeated. Again, almost no S diffusion could be observed in Cr_2O_3. In contrast, slight diffusion into the crucible wall and lid could be seen within SiC. In Fig. 17, this behavior is demonstrated.

The presence of S in the crucible walls and lid, as demonstrated in the SiC trials, suggests that further analysis, such as SEM, is necessary to determine whether new phases have been created or if the observed elements are merely the result of diffusion and infiltration.

While S interaction could lead to potential damage of the refractories, Li has highly destructive capabilities, as shown from results with MgO crucibles. From these results, Li tends to diffuse into the crucible, forming lithium-hydroxide once getting in contact with air humidity when cooled down, leading to severe volume expansion and crack formation. As this phenomenon is likely to occur also within SiC and Cr_2O_3 crucibles, LIBS analyses were compared to investigate the diffusion depth of Li within the two refractory materials. A comparison of this behavior in the different crucibles after trials within the InduMelt reactor is given in Fig. 18.

3.3. Analysis of the microstructure

As seen within Fig. 18 LIBS analyses have shown, that SiC is more prone to Li diffusion with a penetration depth of nine mm, while Cr_2O_3 showed less susceptibility, with a penetration depth of only three mm. As the open porosity of SiC is higher than that of Cr_2O_3, and at the same time the bulk density of Cr_2O_3 is higher than that of SiC, the deeper penetration of Li but also from S into SiC can be easily explained. While the diffusion depth can be described with these two physical properties, further analyses with SEM and XRD should provide additional knowledge about possible reactions between Li and the refractory materials.

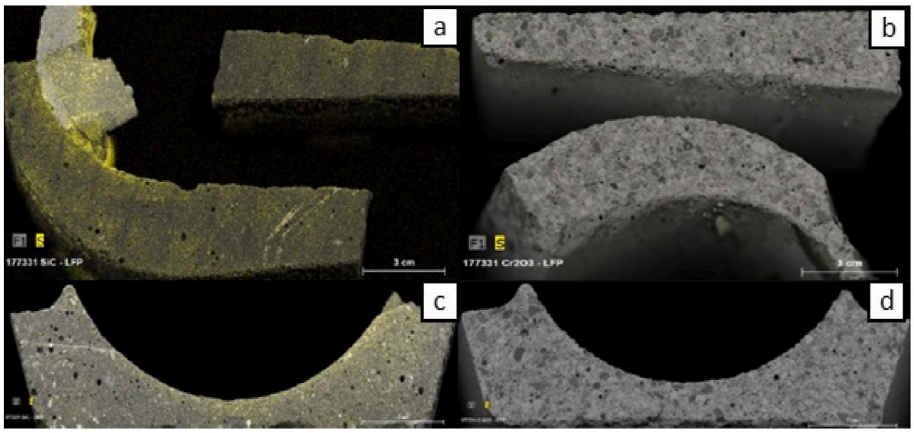

Fig. 17. Diffusion behavior of Sulfur in different crucible materials and areas after trials with the LFP mixture: a.) SiC crucible; b.) Cr_2O_3 crucible; c.) SiC lid; d.) Cr_2O_3 lid.

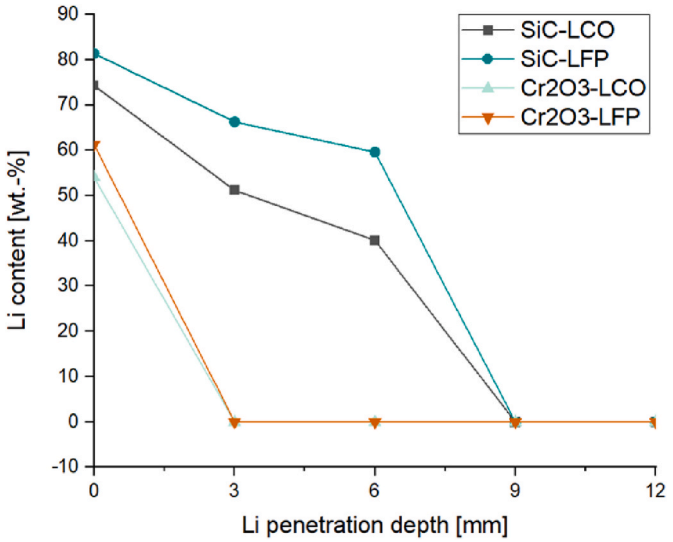

Fig. 18. Li diffusion into different crucibles after carbothermal treatment of LCO and LFP within the InduMelt reactor.

The results of μXRF show an overview of infiltration, corrosion and diffusion areas. However, to analyze what happens on a microscopic level, SEM analyses combined with EDX can show where and how the attack between input material and refractory grains occurs. For a better comparison, Fig. 19 provides a SEM image with corresponding EDX analysis of untreated SiC and Cr_2O_3 crucibles. The SiC crucible shows a highly porous structure with large SiC aggregates, corundum (Al_2O_3) fines and anorthite ($CaAl_2Si_2O_8$) as the bonding phase. The chromite crucible shows a denser matrix made of corundum, chromite, mullite and silica between the large chromite and corundum grains.

To analyze whether the major damage is caused by infiltration and corrosion or by diffusion of both refractory materials, a representative sample of the crucible and the lid was considered for investigation, where the lid only came in contact with gaseous reaction products. Continuing the sequence from the μXRF trials starting with SiC, Fig. 20 shows a reaction zone between the crucible and metallic phase after carbothermal reduction of the LFP mixture. In this figure, the white phase in the upper part represents the metal phase, whereas the lower parts show the refractory with bigger SiC grains and a matrix. Fig. 20a shows a part of the bottom of the crucible where the contact between the liquid metallic phase and refractory was the highest. It is visible that the liquid phases corroded the whole surface up to a depth of about 30 μm. After this depth, there was no more aggressive corrosion. However, Li-rich phases were found up to a depth of 9 mm, indicating a diffusion of either gaseous species or an increased reaction between the refractory and a possible intermediate phase.

On the crucible's inner surface, the SiC grain's dissolution, shown in Fig. 20b, is evident due to contact with the liquid phase. The white spheres are iron phosphides where the iron absorbs the carbon from the SiC. What remains of the grain is a skeleton consisting mainly of lithium aluminosilicates ($LiAlSiO_4$), as seen in the figure and validated by XRD analyses shown in Fig. 21. Next to SiC and $LiAlSiO_4$, iron phosphide (Fe_2P) and calcium magnesium phosphate ($CaMgP_2O_7$) could be found.

Furthermore, the crucible has the most porous structure in the middle compared to the inner and outer contact zones, with metallic phases and oxygen from the air, respectively. The inner crucible wall is denser due to infiltration and partial building of intermediate phases, whereas the outer surface is denser due to the formation of SiO_2, as

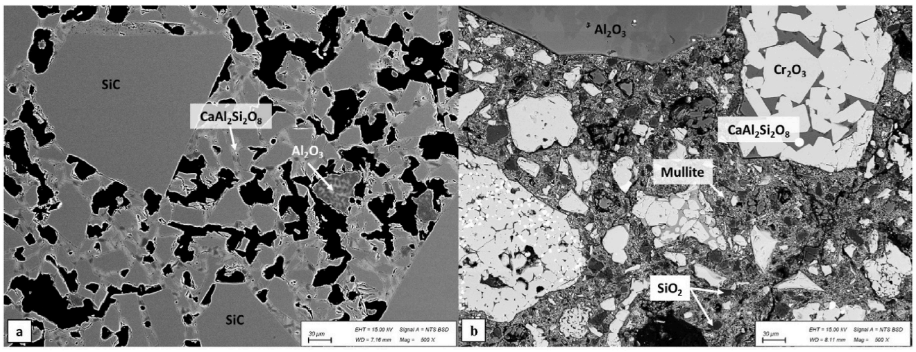

Fig. 19. SEM images of crucibles before carbothermal reduction trials. a.) SiC, b.) Cr2O3.

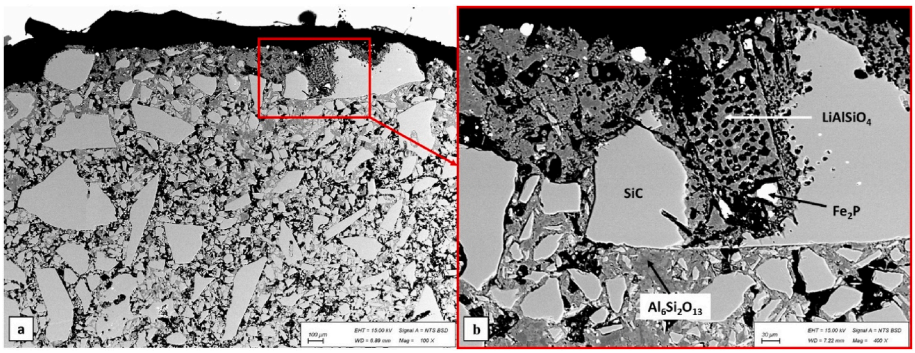

Fig. 20. SEM image of SiC crucible after carbothermal reduction of the LFP mixture with corresponding EDX analysis: a.) low magnification with contact zone between metal phase and crucible; b.) corroded SiC grain with high magnification.

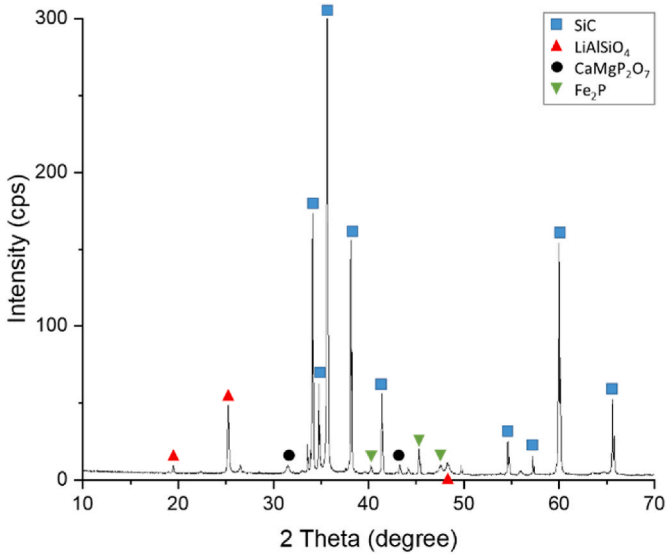

Fig. 21. XRD analysis of the SiC crucible from the inner surface, as seen in Fig. 20.

shown in Formula 2. Between the SiC grains, the matrix consists mainly of mullite ($Al_6Si_2O_{13}$), anorthite ($CaAl_2Si_2O_8$), and occasional $LiAlSiO_4$. Where the crucible was in direct contact with the ceramic fiber blanket, almost no pores were seen with SiC oxidized at the edges and embedded in anorthite, validating the assumption of passive oxidation on the outer surface.

The alloy in Fig. 22a obtained after the test consists mainly of iron phosphides (FeP, Fe_2P, and Fe_3P). The gussets contain copper phosphides (Cu_mP_n) and metallic copper. Some of the phosphides have up to five mol % Si dissolved. Occasionally, dark pores occur, which could contain lithium. The slag in Fig. 22b consists of lithium aluminosilicates ($Li_2Al_2Si_3O_{10}$, $LiAlSi_3O_8$, $LiAlSi_2O_6$). Inclusions of iron phosphides are visible as well. The light-colored gusset phases could not be determined due to their small size. Li_2O and Al_2O_3 from the slag diffuse into the SiC grains of the refractory to from $Li_2Al_2Si_3O_{10}$. This can be easily recognized by the dark edges around the SiC grains.

Compared to the crucible, the lid (Fig. 23) of the SiC crucible shows a largely porous structure. The binding phases between the SiC grains consist of SiO_2-rich glass phases, anorthite, corundum (Al_2O_3) and mullite. On the underside of the lid, denser sintering is visible up to a depth of 400 μm from the inside. Due to the formation of a gas phase, the spherical pores are conspicuous here and could be a sign of gaseous Li diffusing into the crucible. Sintered phases of anorthite, glass phase, and lithium aluminosilicates ($Li_2Al_2Si_3O_{10}$, $LiAlSi_3O_8$, $LiAlSi_2O_6$) are present around the grains.

Compared to SiC, the Cr_2O_3 crucible, shown in Fig. 24, is heaviliy infiltrated with a molten phase. On the inside of the crucible, both chromite and compound grains show broad reaction seams with the formation of spinel through alternating diffusion of one element into the other. Spinels are predominantly present in the matrix, formed by diffusion of Al_2O_3 into the Cr_2O_3 fine grain. Lithium phosphates, lithium-calcium phosphates, and lithium-aluminum silicates ($Li_2Al_2Si_3O_{10}$) are present in the gussets. The reaction seams are less wide on the outside, where the structure is also more porous. However, different lithium phosphates, lithium-aluminum silicates, and lithium-aluminum-phosphate silicates are also present in the matrix.

Looking at the lid of the Cr_2O_3 crucible the porous structure on the outside consists mainly of escolaite (Cr_2O_3) and, to a lesser extent, corundum (Al_2O_3) grains (Fig. 25). Hardly any reaction seams are visible around the large grains. The matrix comprises escoliate, spinel ($(Al, Cr)_2O_3$) and anorthite. Lithium phosphate ($Li_3(PO_4)$) was also detected

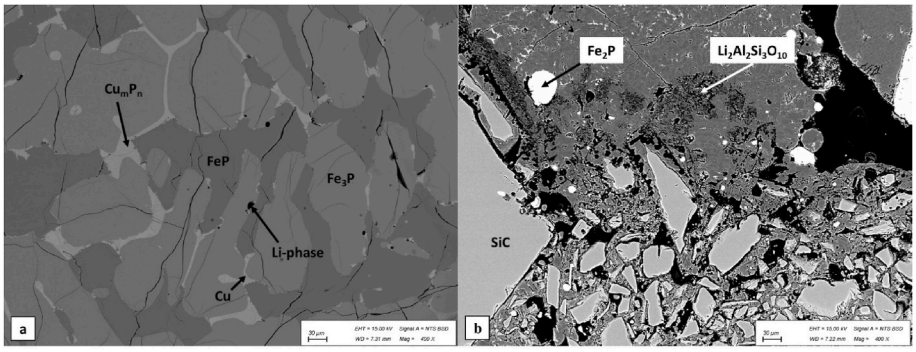

Fig. 22. SEM images of different phases after carbothermal reduction of the LFP mixture in the SiC crucible: a.) metal phase with Cu gussets; b.) interaction zone between crucible and slag phase.

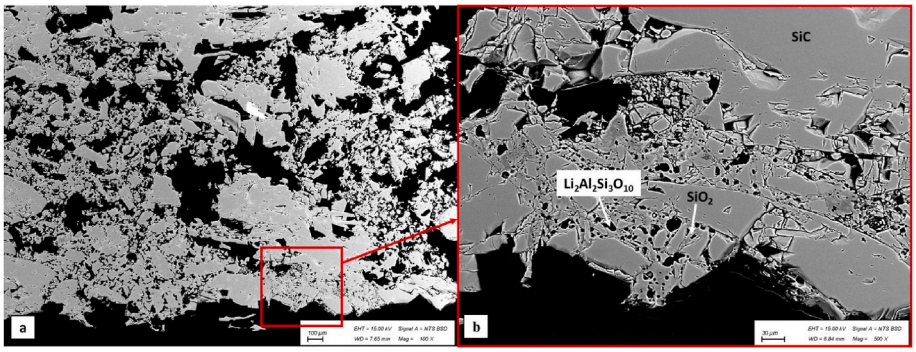

Fig. 23. SEM images of the SiC lid after carbothermal reduction of the LFP mixture: a.) overview of reaction zone on the inner side of the lid in contact with the gas phase; b.) magnification with porous structure.

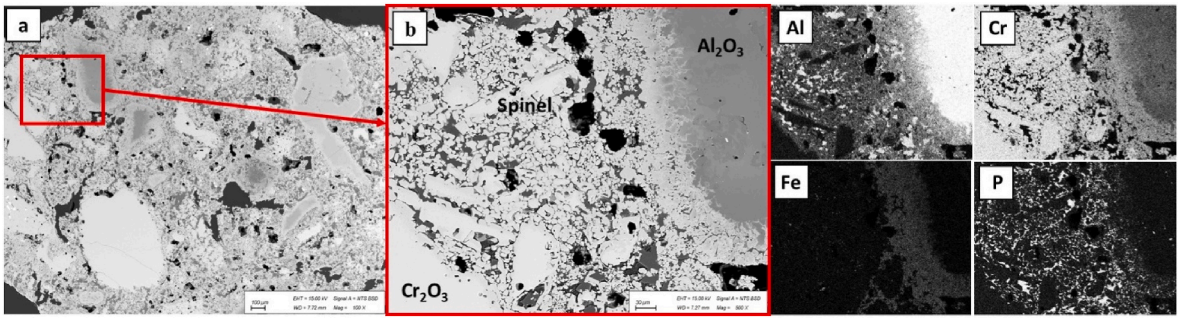

Fig. 24. SEM image of the Cr_2O_3 crucible after carbothermal reduction of the LFP mixture: a.) overview of reaction zone on the inner side of the crucible in contact with the liquid phases; b.) magnification with a partially corroded corundum grain with infiltration of Cr_2O_3; c.) elemental distribution of Cr, Al, Fe, P, Ca and Si.

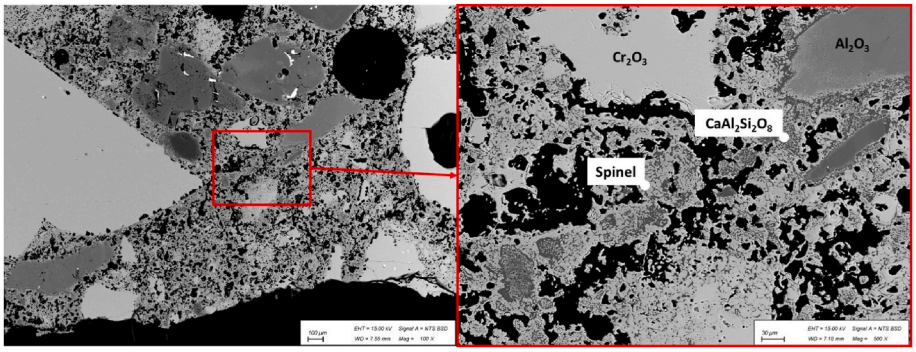

Fig. 25. SEM images of the Cr_2O_3 lid after carbothermal reduction of the LFP mixture: a.) overview of reaction zone on the inner side of the lid in contact with the gas phase; b.) magnification with porous structure.

using XRD. The inside of the lid looks similar, but additional lithium chromium oxides could be detected with XRD.

Looking at the high temperature reactions between the volatile element Li and the remaining components such as alloy, slag and refractory, Li is most probably to be found in the slag, according to Gibbs Energy. Phases such as β-eucryptite ($LiAlSiO_4$), lithium-aluminate (γ-$LiAlO_2$), and lithium-aluminium silicates ($Li_2Al_2Si_3O_{10}$) are most likely to be expected, which was also confirmed by SEM analyses (Figs. 20–23) [44,45]. This complexity makes it quite challenging to recycle lithium effectively in downstream hydrometallurgical approaches, which is why flux formers are avoided within the approach presented in this work. As a result, Li can be expected first to form lithium carbonate (Li_2CO_3) and at higher temperatures lithium oxide (Li_2O), which then evaporates [46]. Once evaporated, due to its high reactivity, Li easily reacts with the refractories, before it can be extracted from the ractor interior. In case of SiC, Li can irreversibly react with SiC to form Li_xSi_yC and Si to a certain extent. The remaining SiC alleviates the volume change, therefore avoiding mechanical failure [47].

4. Conclusion

The extensive research into alternative refractory materials for the InduRed reactor has led to a detailed understanding of their performance under the extreme conditions of the carbothermal reduction process, corrosion and thermal stress when tested with both LCO and LFP mixtures. The initial trials revealed that a carbon content of 19 wt% was insufficient for complete melting, leading to sintering rather than fusion of the metals. While using 17 wt% of C, with aluminum as an even more potent reducing agent, led to a complete melting, further research to find the optimum quantity of reducing agent for each cathode material has to be elaborated in another work.

To evaluate an optimal candidate as refractory material for the

InduRed reactor, standardized tests according to DIN CEN/TS 15418 were performed, emphasizing SiC and Cr_2O_3 as attractive candidates. Contrary, ZrO_2 crucibles, in particular, suffered from severe crack formation caused either by corrosion, thermal stress or most likely a combination of both. ZrO_2 crucibles continued to exhibit significant crack development and corrosive deterioration, especially when in contact with the LCO mixture, reaffirming their unsuitability for high-temperature applications in reducing atmospheres for LIB recycling. Visual inspections, supported by μXRF and LIBS analyses, confirmed the SiC crucibles' integrity, with no significant infiltration of Co, Fe, Cu or P. When considering possible reactions between crucible material and Li, the SiC crucibles showed a deeper diffusion of Li compared to the Cr_2O_3 crucibles with detection up to a depth of 9 mm while Li was found in the Cr_2O_3 crucibles only up to a depth of 3 mm. This can most likely be attributed to physical properties such as lower bulk density compared with higher porosity in comparison to the Cr_2O_3 crucible. The refractoriness of the SiC crucible, however was not affected negatively after the trials with different input materials.

Although the Cr_2O_3 crucible provides a better diffusion barrier against Li and S, the interaction with LFP, in particular, led to notable corrosion and peeling, with iron and phosphorus infiltration, suggesting a reaction between the crucible material and the melt with the formation of carbides and elemental Cr due to carbothermal reduction. The trials also highlighted the susceptibility of Cr_2O_3 to cracking and severe damage, especially at the bottom of the reactor. This ultimately led to the crucible's failure, resulting in partial leakage and escape of the molten metal.

Looking at all these findings, a reactor for a continuous operation could consist of different areas made of different refractory materials. While the degasification zone could utilize properties of Cr_2O_3, such as minimal diffusion, areas with a more intense contact between the crucible and melt, could utilize the corrosion resistance of SiC. Also, combining a base Cr_2O_3 crucible with a protective layer of SiC could benefit from the advantages of both materials. Furthermore, protective layers such as carbon could be possible solutions for the increased Li and S diffusion within SiC. Concepts such as freeze lining or surface impregnation could decrease Li and S diffusion while preventing refractory wear.

In conclusion, SiC stands out as a promising refractory material for the InduRed reactor, withstanding the corrosive and thermal demands of the process. These findings provide a solid foundation for selecting and optimizing refractory materials in metallurgical processes involving battery materials. Still they also underscore the need for ongoing research. Especially, further research into the behavior of the mechanical strength after multiple test cycles could provide valuable insights into whether SiC or a combination of SiC and Cr_2O_3 can also be used in a continuously operated reactor.

CRediT authorship contribution statement

Lukas Wiszniewski: Writing – review & editing, Writing – original draft, Visualization, Project administration, Methodology, Investigation, Formal analysis, Conceptualization. **Irmtraud Marschall:** Writing – original draft, Investigation. **Thomas Hochsteiner:** Investigation. **Thomas McFarlane Hoad:** Writing – original draft, Investigation. **Klaus Doschek-Held:** Writing – review & editing, Supervision. **Harald Raupenstrauch:** Supervision.

Declaration of competing interest

The authors declare that they have no known competing financial interests or personal relationships that could have appeared to influence the work reported in this paper.

Acknowledgement

Thanks to Fritz Kittinger, Chair of Process Technology and Environmental Protection at Montanuniversität Leoben, for supporting LIBS analyses. Furthermore, a huge appreciation belongs to Hartwig Kunanz and Viktoria Reiter from RHI Magnesita GmbH for providing the required crucible material, μXRF analyses and professional advice. The authors gratefully acknowledge the funding support of K1-MET GmbH, the metallurgical competence centre. The Module FuLIBatteR (Grant number: FO999888343) is supported by COMET (Competence Center for Excellent Technologies), the Austrian programme for competence centres. COMET is funded by the Federal Ministry for Climate Action, Environment, Energy, Mobility, Innovation and Technology, the Federal Ministry for Labour and Economy, the Federal States of Upper Austria and Styria as well as the Styrian Business Promotion Agency (SFG). Furthermore, Upper Austrian Research GmbH continuously supports the module. Besides the public funding from COMET, this research projectis partially financed by the company partners Audi, BRAIN Biotech, Ebner Industrieofenbau, RHI Magnesita, Saubermacher, TÜV SÜD Landesgesellschaft Österreich, VTU Engineering, and voestalpine High-Performance Metals, and the scientific partners acib, CoventryUniversity, Montanuniversität Leoben, University of Natural Resources and Life Sciences, and UVR-FIA.

References

[1] V.M. Leal, J.S. Ribeiro, E. Coelho, M. Freitas, Recycling of spent lithium-ion batteries as a sustainable solution to obtain raw materials for different applications, J. Energy Chem. 79 (2023) 118–134, https://doi.org/10.1016/j.jechem.2022.08.005.

[2] G. Harper, R. Sommerville, E. Kendrick, L. Driscoll, P. Slater, R. Stolkin, A. Walton, P. Christensen, O. Heidrich, S. Lambert, et al., Recycling lithium-ion batteries from electric vehicles, Nature 575 (2019) 75–86, https://doi.org/10.1038/s41586-019-1682-5.

[3] L. Reinhart, D. Vrucak, R. Woeste, H. Lucas, E. Rombach, B. Friedrich, P. Letmathe, Pyrometallurgical recycling of different lithium-ion battery cell systems: economic and technical analysis, J. Clean. Prod. 416 (2023) 137834, https://doi.org/10.1016/j.jclepro.2023.137834.

[4] J.C.-Y. Jung, P.-C. Sui, J. Zhang, A review of recycling spent lithium-ion battery cathode materials using hydrometallurgical treatments, J. Energy Storage 35 (2021) 102217, https://doi.org/10.1016/j.est.2020.102217.

[5] S. Windisch-Kern, A. Holzer, C. Ponak, H. Raupenstrauch, Pyrometallurgical lithium-ion-battery recycling: approach to limiting lithium slagging with the InduRed reactor concept, Processes 9 (2021) 84, https://doi.org/10.3390/pr9010084.

[6] New EU regulatory framework for batteries - Setting sustainability requirements, EPRS - European Parliamentary Research Service, 2023.

[7] X.-Q. Wang, M. Qin, N.-C. Moldovan, C.-W. Su, Bubble behaviors in lithium price and the contagion effect: an industry chain perspective, Resour. Pol. 83 (2023) 103725, https://doi.org/10.1016/j.resourpol.2023.103725.

[8] H. Raupenstrauch, s. Windisch, C. Ponak, V. Mally, A. Holzer, A. Schönberg, Apparatus and process for thermal treatment of raw material containing lithium compounds and phsophorous compounds, method of recovering lithium and/or phsophorous from residual material of lithium-ion batteries, February 25, 2021.

[9] A. Holzer, L. Wiszniewski, S. Windisch-Kern, H. Raupenstrauch, Optimization of a pyrometallurgical process to efficiently recover valuable metals from commercially used lithium-ion battery cathode materials LCO, NCA, NMC622, and LFP, Metals 12 (2022) 1642, https://doi.org/10.3390/met12101642.

[10] Y. Murakami, Y. Matsuzaki, T. Kamimura, T. Nishiura, K. Masuda, A. Shibayama, R. Inoue, Erosion mechanism of refractories in a pyro-processing furnace for recycling lithium-ion secondary batteries, Ceram. Int. 46 (2020) 9281–9288, https://doi.org/10.1016/j.ceramint.2019.12.182.

[11] A. Holzer, S. Windisch-Kern, C. Ponak, H. Raupenstrauch, A novel pyrometallurgical recycling process for lithium-ion batteries and its application to the recycling of LCO and LFP, Metals 11 (2021) 149, https://doi.org/10.3390/met11010149.

[12] H. Itoh, H. Miyanaga, M. Kamiya, R. Sasai, Recovery of rare metals from spent lithium ion cells by hydrothermal treatment and its technology assessment, in: V. Popov (Ed.), Waste Management and the Environment III, WIT, Southampton, 2006, pp. 3–12. ISBN 1845641736, WASTE MANAGEMENT 2006, Malta, 6/21/2006 - 6/23/2006.

[13] M. Soltanieh, A. McLean, Thermodynamics of cobalt aluminate formation in molten cobalt, Steel Res. Int. 76 (2005) 372–376, https://doi.org/10.1002/srin.200506024.

[14] A. Holzer, Investigation of the Phenomena occurring in an inductively heated packed bed reactor for the pyrometallurgical recovery of valuable metals from lithium-ion batteries, Montanuniversität Leoben, 2023.

[15] W.E. Lee, S. Zhang, Melt corrosion of oxide and oxide–carbon refractories, Int. Mater. Rev. 44 (1999) 77–104, https://doi.org/10.1179/095066099101528234.
[16] F. Harders, Feuerfestkunde: Herstellung, Eigenschaften und Verwendung feuerfester Baustoffe, Springer Berlin Heidelberg, Berlin, Heidelberg, 1960. ISBN 9783662117415.
[17] X. Duan, H. Zheng, Y. Chen, F. Qian, G. Liu, X. Wang, Y. Si, Study on the corrosion resistance of cordierite-mullite and SiC refractories to Li-ion ternary cathode materials, Ceram. Int. 46 (2020) 2829–2835, https://doi.org/10.1016/j.ceramint.2019.09.275.
[18] G. Qu, J. Yang, Y. Wei, S. Zhou, B. Li, H. Wang, Mechanism for metal loss in smelting of recycled spent lithium-ion batteries: the overlooked role of refractory materials, J. Environ. Manag. 349 (2024) 119438, https://doi.org/10.1016/j.jenvman.2023.119438.
[19] G. Routschka, H. Wuthnow, in: Praxishandbuch Feuerfeste Werkstoffe: Aufbau, Eigenschaften, Prüfung, 6, Auflage; Vulkan Verlag: Essen, 2017. ISBN 9783802731686.
[20] DIN 51060:2000-06, Feuerfeste keramische Rohstoffe und feuerfeste Erzeugnisse_-Definition der Begriffe feuerfest, hochfeuerfest; Beuth Verlag GmbH: Berlin.
[21] Praxishandbuch feuerfeste Werkstoffe: Aufbau - Eigenschaften - Prüfung; E-Book: das komplette Buch als PDF, Aufl. [der gedr. Ausg.]; Vulkan-Verl.: Essen 5 (2011). ISBN 9783802731617.
[22] T. Beckert, Leitfaden zur Eisenhüttenkunde: Die feuerfesten Baustoffe, Zweite vollständig umgearbeitete Auflage, Springer Berlin Heidelberg, Berlin, Heidelberg, 1898. ISBN 9783642913815.
[23] C.A. Schacht (Ed.), Refractories Handbook, CRC Press, Boca Raton, Fla, 2004. ISBN 0824756541.
[24] DIN CEN/TS 15418:2006-09, Prüfverfahren für dichte feuerfeste Erzeugnisse_-Leitlinien zur Prüfung von durch Flüssigkeiten hervorgerufene Korrosion an feuerfesten Erzeugnissen; Deutsche Fassung CEN/TS_15418:2006; Beuth Verlag GmbH: Berlin.
[25] B. Ertuğ, Classification and characteristics of predominant refractories used in metallurgy, AEF 26 (2018) 9–21. www.scientific.net/AEF.26.9.
[26] S. Gschiel, S. Eder, N. Freiberger, C. Bauer, A novel raw material developed for slide gate plate technology, RHI Bulletin (2021) 36–41. Available online: https://www.rhimagnesita.com/wp-content/uploads/2021/09/bulletin-2021.pdf (Accessed 7 February 2024).
[27] A. Holzer, J. Zimmermann, L. Wiszniewski, T. Necke, C. Gatschlhofer, W. Öfner, H. Raupenstrauch, A combined hydro-mechanical and pyrometallurgical recycling approach to recover valuable metals from lithium-ion batteries avoiding lithium slagging, Batteries 9 (2023) 15, https://doi.org/10.3390/batteries9010015.
[28] Elevator furnaces | Thermconcept ofenlösungen, Available online, https://www.thermconcept.com/virthos.php?en//Produkte/Forschung/20/26/20Labor/Elevator/C3/B6fen/Elevator/C3/B6fen. (Accessed 23 February 2024).
[29] E.L. Pang, G.B. Olson, C.A. Schuh, The mechanism of thermal transformation hysteresis in ZrO_2 - CeO_2 shape-memory ceramics, Acta Mater. 213 (2021) 116972, https://doi.org/10.1016/j.actamat.2021.116972. ISSN 1359-6454.
[30] J.T. Slycke, E.J. Mittemeijer, M. Somers, Thermodynamics and kinetics of gas and gas–solid reactions, in: E.J. Mittemeijer, M.A.J. Somers (Eds.), Thermochemical Surface Engineering of Steels: Improving Materials Performance, Woodhead Publishing, Cambridge, Massachusetts, 2015, pp. 3–111. ISBN 978-0-85709-592-3.
[31] Micro-XRF, TU wien, Available online: https://www.tuwien.at/phy/ati/strahlenphysik/forschung/roentgenphysik/angewandte-methoden/micro-xrf. (Accessed 7 February 2024).
[32] LIBS LaLibs | TU wien, Available online: https://www.tuwien.at/tch/lalibs/technliken/libs. (Accessed 7 February 2024).
[33] T.D.T. Oyedotun, X-ray fluorescence (XRF) in the investigation of the composition of earth materials: a review and an overview, Geology, Ecology, and Landscapes 2 (2018) 148–154, https://doi.org/10.1080/24749508.2018.1452459.
[34] C. Bauer, B. Rollinger, G. Krumpel, O. Hoad, J. Pascual, N. Rogers, H. Dösinger, Characterization methods to investigate zirconia phase transformations in slag bands, Available online: https://www.rhimagnesita.com/wp-content/uploads/2017/10/RHI_Bulletin_2016-01-data.pdf, 2016. (Accessed 7 February 2024).
[35] L. Wiszniewski, T. Hochsteiner, A. Fercher, H. Raupenstrauch, Influence of impurities such as C, Al and Cu on the melting behavior of LIB cathode materials under inert and reducing atmospheres, Zenodo, 2023.
[36] L. Huang, T. Lu, G. Xu, X. Zhang, Z. Jiang, Z. Zhang, Y. Wang, P. Han, G. Cui, L. Chen, Thermal runaway routes of large-format lithium-sulfur pouch cell batteries, Joule 6 (2022) 906–922, https://doi.org/10.1016/j.joule.2022.02.015.
[37] R.G. Munro, S.J. Dapkunas, Corrosion characteristics of silicon carbide and silicon nitride, J. Res. Natl. Inst. Stand. Technol. 98 (1993) 607–631, https://doi.org/10.6028/jres.098.040.
[38] W.L. Vaughn, H.G. Maahs, Active-to-Passive transition in the oxidation of silicon carbide and silicon nitride in air, J. Am. Ceram. Soc. 73 (1990) 1540–1543, https://doi.org/10.1111/j.1151-2916.1990.tb09793.x.
[39] E.A. Gulbransen, K.F. Andrew, F.A. Brassart, The oxidation of silicon carbide at 1150° to 1400°C and at 9 × 10[sup −3] to 5 × 10[sup −1] torr oxygen pressure, J. Electrochem. Soc. 113 (1966) 1311, https://doi.org/10.1149/1.2423812.
[40] F.F. Lange, Healing of surface cracks in SiC by oxidation, J. Am. Ceram. Soc. 53 (1970) 290, https://doi.org/10.1111/j.1151-2916.1970.tb12104.x.
[41] M.E. Schlesinger, The thermodynamic properties of phosphorus and solid binary phosphides, Chem. Rev. 102 (2002) 4267–4301, https://doi.org/10.1021/cr000039m.
[42] T. Mori, J. Yang, M. Kuwabara, Mechanism of carbothermic reduction of chromium oxide, ISIJ Int. 47 (2007) 1387–1393, https://doi.org/10.2355/isijinternational.47.1387.
[43] R.E. Kryukov, V.F. Goryushkin, Y.V. Bendre, L.P. Bashchenko, N.A. Kozyrev, Thermodynamic aspects of Cr2O3 reduction by carbon, Steel Transl. 49 (2019) 843–847, https://doi.org/10.3103/S0967091219120052.
[44] T. Schirmer, H. Qiu, H. Li, D. Goldmann, M. Fischlschweiger, Li-distribution in compounds of the Li2O-MgO-Al2O3-SiO2-CaO system—a first survey, Metals 10 (2020) 1633, https://doi.org/10.3390/met10121633.
[45] H. Li, H. Qiu, M. Ranneberg, H. Lucas, T. Graupner, B. Friedrich, B. Yagmurlu, D. Goldmann, J. Bremer, M. Fischlschweiger, Enhancing lithium recycling efficiency in pyrometallurgical processing through thermodynamic-based optimization and design of spent lithium-ion battery slag compositions, ACS Sustainable Resour. Manage. (2024), https://doi.org/10.1021/acssusresmgt.4c00064.
[46] A.N. Timoshevskii, M.G. Ktalkherman, V.A. Emel'kin, B.A. Pozdnyakov, A. P. Zamyatin, High-temperature decomposition of lithium carbonate at atmospheric pressure, High Temp. 46 (2008) 414–421, https://doi.org/10.1134/S0018151X0803019X.
[47] X.D. Huang, F. Zhang, X.F. Gan, Q.A. Huang, J.Z. Yang, P.T. Lai, W.M. Tang, Electrochemical characteristics of amorphous silicon carbide film as a lithium-ion battery anode, RSC Adv. 8 (2018) 5189–5196, https://doi.org/10.1039/C7RA12463E.